Characterization of uranium redox state in organic-rich Eocene sediments

Susan A Cumberland[1,2,3], Barbara Etschmann[2], Joël Brugger[2], Grant Douglas[4], Katy Evans[5], Louise Fisher[6], Peter Kappen[3], John W. Moreau[1]

1 School of Earth Sciences, University of Melbourne, Parkville, Victoria 3100, Australia

2 School of Earth, Atmosphere and Environment, Monash University, Clayton 3800, Victoria, Australia

3 ANSTO Australian Synchrotron, 800 Blackburn Road, Clayton 3168, Victoria, Australia

4 CSIRO Land and Water, Floreat, Western Australia, Australia

5 Western Australian School of Mines, Curtin University, Bentley, Western Australia, Australia

6 CSIRO Mineral Resources, Bentley, Western Australia, Australia

Abstract

The presence of organic matter (OM) has a profound impact on uranium (U) redox cycling, either limiting or promoting the mobility of U via binding, reduction, or complexation. To understand the interactions between OM and U, we characterised U oxidation state and speciation in nine OM-rich sediment cores (18 samples), plus a lignite sample from the Mulga Rock polymetallic deposit in Western Australia. Uranium was unevenly dispersed within the analysed samples with 84% of the total U occurring in samples containing >21 wt. % OM. Analyses of U speciation, including x-ray absorption spectroscopy and bicarbonate extractions, revealed that U existed predominately (~71%) as U(VI), despite the low pH (4.5) and nominally reducing conditions within the sediments. Furthermore, low

extractability by water, but high extractability by a bi-carbonate solution, indicated a strong association of U with particulate OM. The unexpectedly high proportion of U(VI) relative to U(IV) within the OM-rich sediments implies that OM itself does not readily reduce U, and the reduction of U is not a requirement for immobilising uranium in OM-rich deposits. The fact that OM can play a significant role in limiting the mobility and reduction of U(VI) in sediments is important for both U-mining and remediation.

Keywords: Mulga Rock, uranium, mobility, organic matter, oxidation state, x-ray absorption spectroscopy.

Highlights

- 84% of U in Mulga Rock OM-bearing sediments occurred within the OM-richest samples (>21% total organic carbon; 9 of 18 samples).
- 71% of U was present in the U(VI) oxidation state.
- Higher proportions of U occur as U(VI) in mature OM-rich sediments than previously thought.
- OM strongly complexes U(VI), limiting its mobility and reactivity.
- U reduction processes are not ubiquitous within OM-rich sediments.

1 Introduction

The mobility of uranium (U) in natural environments is controlled by its oxidation state and solubility, with the uranyl ion ($U^{VI}O_2^{2+}$) generally more soluble than U(IV). Ligands such as CO_3^{2-}, OH^-, PO_4^{3-} and SO_4^{2-} can either increase (via formation of stable aqueous complexes) or decrease (via formation of insoluble minerals) U mobility (Cumberland et al., 2016). Uranium mobility is also influenced by organic matter (OM) in both dissolved and colloidal/particulate forms (Wood, 1996; Cumberland et al., 2016). Depending on pH,

47 dissolved OM such as humic and fulvic acids can bind U, facilitate its transportation, and
48 prevent its sorption to mineral surfaces (Luo and Gu, 2008; Zhao et al., 2012; Tinnacher et
49 al., 2013). In contrast, particulate or solid phase OM can adsorb and accumulate U, resulting
50 in the formation of OM-rich sedimentary U deposits (Greenwood et al., 2013; Cumberland
51 et al., 2016). While considerable information exists on U mobility in inorganic systems
52 (Grenthe et al., 2004), datasets for organic-rich systems are comparatively deficient (Bargar
53 et al., 2013). The complex molecular-scale associations of U and OM, and the impact of OM
54 on U mobility/immobilisation, are still being unravelled (Bargar et al., 2013). These
55 knowledge gaps limit development of *in situ* mining technologies (Zammit et al., 2014), as
56 well as environmental management and remediation strategies for U mining sites.

57 Recent studies have been directed towards understanding U mobility in OM-rich modern
58 sediments, including the pathways through which U potentially accumulates (Tokunaga et
59 al., 2005; Law et al., 2011). Peat, for example, can concentrate U by up to factor of 10,000
60 from groundwater containing ppb level U concentrations (e.g. (Idiz et al., 1986; Read et al.,
61 1993; Owen and Otton, 1995; Lidman et al., 2012)). Bryan et al. (2012) and Warwick et al.
62 (2005) identified U sorption to carboxylic and phenolic functional groups on insoluble
63 humics and fulvics as the likely scavenging mechanism. Furthermore, U accumulation in
64 peat and other OM-rich environments is commonly conceptualised as involving initial U(VI)
65 adsorption followed by reduction to U(IV), with the latter process resulting in long-term U
66 immobilisation (Spirakis, 1996). A suite of factors may facilitate U reduction in sediments,
67 including increased temperature (Nakashima 1992), electron donors such as H_2S or Fe^{2+}, and
68 direct enzymatic reduction (Newsome et al., 2014; Campbell et al., 2015). Mineral surfaces
69 (e.g., pyrite; Fe-Ti-oxides) and insoluble OM may also play roles in reduction of sorbed U(VI),

70 catalysing rate-limiting reaction steps by facilitating electron transfer from underlying
71 material or co-adsorbates (Renock et al., 2013; Latta et al., 2014). Most U in fossil economic
72 U deposits, including OM-rich types (Min et al., 2000; Deditius et al., 2008), has been
73 assumed to be associated with U(IV)-minerals, such as coffinite, or other non-crystalline
74 forms (Bhattacharyya et al., 2017). Interestingly, synchrotron X-ray absorption spectroscopy
75 (XAS) data have revealed the presence of both U(IV) and U(VI) in some OM-rich U deposits,
76 with U(IV) constituting of 35-68% of total U (Mikutta et al., 2016). Regenspurg et al. (2010)
77 found a mixture of U(VI) and U(IV) in alpine soils from the Dischma Valley (Switzerland),
78 based on combined carbonate extractions and data from X-ray Absorption Near Edge
79 Structure (XANES) analyses. These results point to U(VI) being an important component of
80 U bound to OM surfaces. From these recent findings, a picture is emerging for U-OM
81 association in modern sediments that emphasizes the complexity and variability of U redox
82 state and chemical speciation (Mikutta et al., 2016; Bone et al., 2017).

83 Synchrotron x-ray absorption spectroscopy (XAS) provides a suitable analytical technique for
84 obtaining U-oxidation state and speciation in OM-rich sediments, since it is sensitive to both
85 'invisible' (e.g., colloidal; adsorbed; associated with OM, typically sub > 10 nm) and mineral-
86 bound U (Denecke et al., 1998a; Denecke et al., 1998b; Mikutta et al., 2016; Bhattacharyya
87 et al., 2017). XAS can be applied to samples with a complex composition and containing a
88 wide range of U concentrations (from a few ppm to wt.%). Here our objective was to
89 characterise the physical and chemical nature of U within an OM-rich Eocene sedimentary U
90 deposit, Mulga Rock (Western Australia), in order to determine the relative abundance and
91 origins of observed U(IV) or U(VI). Our results inform strategies for sustainable mining

(subsurface extraction) or environmental remediation of U in OM-rich sedimentary or aqueous environments.

2 Geological setting and core sampling

The Mulga Rock (MR) U deposit is located near Kalgoorlie (Western Australia; Figure 1), hosted within a series of paleochannels and lacustrine beds formed during the Eocene (56-34 Ma), now buried to shallow depths (30 to 50 m). According to the petrographic analyses of Jaraula et al. (2015), MR sediments contain a mixture of particulate and non-particulate OM consisting of woody (lignite) material combined with aquatic algal and bacterial biomass, consistent with accumulation from a combination of forested, wetland and lacustrine environments. Over time, the OM layers and deeper sediments became anoxic, with considerable evidence for microbial production of authigenic minerals, most prominently Fe-sulphides. Uranium accumulation likely resulted from groundwater flow through permeable sandstones within palaeochannels, and scavenging of the carried U (present day average 8 $\mu g\ L^{-1}$ U in local groundwater) by OM-rich layers (Douglas et al., 2011; Jaraula et al., 2015). U-Pb isotope systematics and U-Th disequilibria studies suggest that U and the associated metals originated from local lamproitic or carbonatitic sources (Douglas et al., 2011; Jaraula et al., 2015).

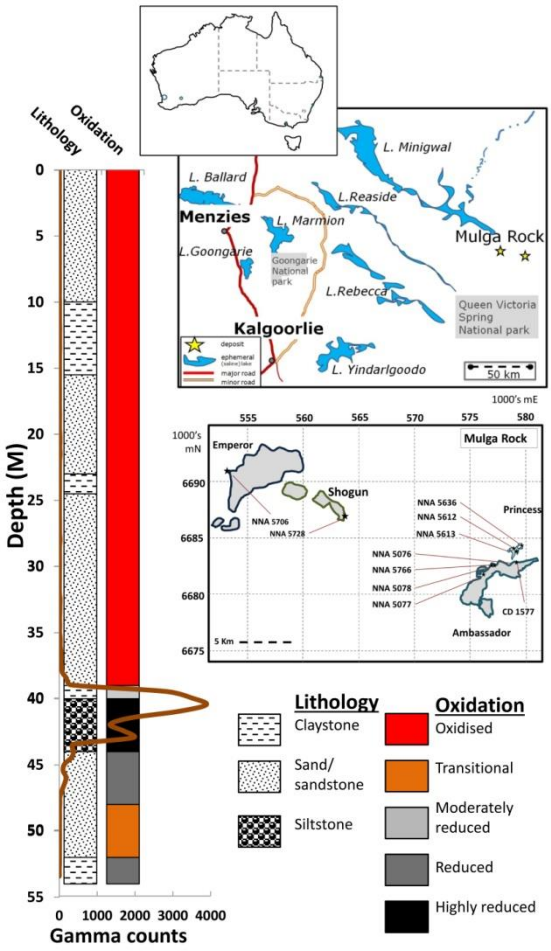

Figure 1. Map of Mulga Rock, deposit sites, core locations and detail from core 5613 showing lithology, oxidation state and radioactivity (obtained from down-hole gamma log counts (Vimy, 2014)). See also SI Table 1 for locations.

To date, four orebodies with potential U resources have been delineated at MR: Ambassador, Emperor, Princess and Shogun (Figure 1). Ambassador, discovered in 1979, has been the main subject of industry and academic investigations, with resources estimated at 13,000 tonnes U (Douglas et al., 1993; Douglas et al., 2011). The most recent orebody, Princess, was discovered in March 2012. The wider MR deposit is estimated to contain 66.5 MT of ore at 520 mg kg^{-1} U_3O_8 (Vimy, 2016c). The geological setting and close association of U with OM-rich sediments at MR make it an excellent site for studying the nature of U in ore-grade OM-rich environments.

We analysed 18 samples from nine air- and diamond-drilled cores obtained from the March 2012 drilling project: Ambassador (4), Emperor (1), Princess (3) and Shogun (1), together with a section of lignite (CD 1577) extracted during a previous exploration campaign from the Ambassador deposit (Vimy, 2014, 2015, 2016a, b). Lignite sample CD 1577 was immediately preserved in epoxy resin to prevent oxidation. The March 2012 samples were selected on-site as they were extracted (sample locations given in **Error! Reference source not found.**) and immediately stored in airtight containers, taking care to minimize exposure to air and to leave no air gap. The samples were selected to represent a range of redox states, mineralisation types and grades, as estimated on-site by a handheld Niton XL3t X-ray Fluorescence (XRF) spectrometer, and on the radiometrics determined using a down-hole gamma probe (AusLog, #T125, 33mm diameter) calibrated with a Cs^{137} source (Vimy, 2014, 2016b). Laboratory based geochemical analysis was completed 6-12 months after sampling and preservation; synchrotron X-ray analysis was performed within two years of sample preservation.

3 Geochemical Analysis

Six analytical methods were used: bulk core sample analysis (ICP-MS); chemical extractions (ICP-MS); electron microscopy; and synchrotron-based XAS and X-ray fluorescence microscopy (XFM).

3.1 Sample preparation and measurements of loss on ignition (LOI) and pH

Samples were characterised using fresh, oven-dried, ashed or dried-homogenised material. To obtain dry masses, sub-samples and replicates were oven-dried at least overnight at 104 ^{o}C and weighed until constant mass. The resulting oven-dried samples either underwent LOI analysis, or were homogenised to a very fine powder in an agate-lined ball mill and dry-

145 stored in glass vials at ambient temperatures until further analysis. The LOI analysis was
146 undertaken on a subset of samples (replicates = 5, n = 12) at 550 ^{o}C for 4 hr, then 900 ^{o}C for
147 2 hr, using a Thermoline muffle furnace (Dean, 1974; Heiri et al., 2001). A reduced number
148 of samples were analysed for LOI (12 of 18) to conserve material. Powdered samples were
149 analysed for total nitrogen (TN), organic carbon (TOC) and sulphur (TS) by an Elementar III
150 Elemental Analyser (University of Kiel) without further pre-treatment. Sediment pH was
151 analysed within 3 months of sample recovery using the method of (Rowell, 1994).
152 Measurements were conducted on duplicate samples using a Thermo portable meter with
153 standard calomel electrode. Six grams of undried sample was mixed with 15 ml of water, the
154 slurry was shaken by hand for 15 minutes, and the pH was then measured immediately and
155 again after 10 minutes.

156 ### 3.2 Total and extractable metals including U

157 Total metals, U and rare earth elements (REE) concentrations were obtained from acid-
158 digested samples using a method adopted from Kamber et al. (2003) and Eggins et al.
159 (1997). Both dried and ashed samples were analysed for U (SI Table 5). 2 mL of triple-
160 distilled HF and 1 mL triple-distilled HNO_3 were added to 100 mg of sample in capped Teflon
161 vessels and digested at 135 ˚C overnight on a hotplate. The dehydrated material was
162 refluxed twice with concentrated HNO_3, then dissolved overnight in 3N HNO_3. The solutions
163 were transferred to transparent polycarbonate tubes, and diluted with water. Solutions
164 were diluted further to a factor of 5000 with a solution of 1.6 % HNO_3, then analysed using
165 inductively coupled plasma-mass spectrometry (quadrupole ICP-MS, *Agilent 7700x*). Results
166 of digested samples are reported as mg kg^{-1} of dry mass. There was a significant correlation
167 (R^2 = 0.999, $p < 0.005$) between the ashed (n=12) and unashed samples, indicating
168 confidence in that the organic matrix did not interfere with the ICP-MS analysis.

169 Bi-carbonate (HCO_3^-) (Zhou and Gu, 2005) and pure water extractions (ultra pure, 18.2 MΩ)
170 were undertaken to further constrain U speciation and oxidation state on 18 sub-samples.
171 Typically, bi-carbonate extraction assumes that in the absence of oxygen, U(VI) forms strong
172 complexes with carbonate ions and hence becomes highly soluble, whereas U(IV), including
173 unoxidised biogenic U(IV), remains uncomplexed and insoluble (Guillaumont et al., 2003;
174 Zhou and Gu, 2005). In some circumstances, monomeric (i.e., sorbed) biogenic U(IV) can be
175 released in concentrated bicarbonate solutions, without affecting uraninite/coffinite
176 stability (Alessi et al., 2012). Thus in our work the extracted U(VI) may also contain a small
177 fraction of mobile, highly reactive biogenic U(IV). The dissolved U(VI) can be separated by
178 filtration (i.e. 0.2 µm) of the aqueous phase, and the U(IV) concentration can be estimated
179 by subtraction of the amount of soluble U analysed by ICP-MS from the total U value. This
180 provides a minimum U(VI) concentration, since some U(VI) minerals, in particular silicates,
181 phosphates and vanadates are sparingly soluble (Tokunaga et al., 2012; Kanematsu et al.,
182 2014; Mehta et al., 2014). Bi-carbonate extractions were performed in duplicate under
183 anaerobic (N_2) conditions as follows: 20 ml of 1 M $NaHCO_3$ (de-gassed) was added to ~1.7 g
184 fresh hand-ground sediment; pH was recorded; and the sample was placed in 100 mL
185 crimped and sealed serum bottles (acid washed, 10% HNO_3) with the headspace replaced
186 with N_2 gas to avoid oxidation. Blanks were prepared as above. The suspensions were
187 rotated on an orbital shaker (150 rpm, 25 ^oC) continuously for one week, and then settled
188 for 10 minutes, after which they were vacuum-filtered through 0.2 µm cellulose nitrate
189 membranes (*Whatman*). Filtration was generally fast, with additional filters used where
190 necessary. Filtrate solutions were acidified (1% HNO_3) and then analysed by ICP-MS. The pH
191 of the bi-carbonate/sediment suspension was 8.5 ± 0.1. Water extractions were performed

under the same conditions but filtered using a standard 1.2 μm GF/C Whatman glass filter paper to include a potentially mobile U colloidal fraction.

3.3 Imaging U distribution and elemental association using XFM and SEM

To determine the microscale spatial distribution and elemental/mineralogical association of U, subsamples of unground grains from core NNA 5613 (Ambassador ore body) were selected based on total activity (measured by Geiger counter) and mounted onto 0.5 cm^2 SiN windows using a 5% glucose solution. Due to the finely dispersed nature of the U in the MR samples, TEM techniques proved unsuccessful in detecting U in the samples. One sample, MR5613a, yielded better SEM results and gave higher radioactive counts per second, likely due to higher U (5000 mg kg^{-1}) concentrations. This sample was therefore favoured for subsequent micro-analytical characterisation.

Subsample grains from MR5613a were analysed at the XFM Beamline (Australian Synchrotron) at 18.5 keV incident photon energy and 2 μm beam size (Paterson et al., 2011). Fluorescence signals were collected using a 384-pixel Maia detector (Ryan et al., 2014). The fluorescence spectra collected were processed using the GeoPIXE software to produce semi-quantitative elemental maps (Ryan and Jamieson, 1993; Ryan, 2000; Etschmann et al., 2010; Li et al., 2016).

Backscatter electron images (sample MR5613a from core NNA 5613) were obtained on thin sections using a Philips FEI XL30 environmental scanning electron microscope (ESEM) equipped with an OXFORD INCA energy-dispersive X-ray spectrometer (EDS) (Earth Sciences, University of Melbourne), and EDS maps were collected with a Field Emission Philips XL30 ESEM (BIO21, University of Melbourne).

The mineralogy of lignite sample CD 1577 was characterised using µ-XRD. Spectra were collected using a Bruker general area detector diffraction system (GADDS) with Cu K_α radiation and 200 or 300 µm collimators (CSIRO, Clayton, Melbourne; SI Figure 1).

3.4 Uranium speciation via XANES and EXAFS spectroscopy.

X-ray absorption near edge structure (XANES) and extended x-ray absorption fine structure (EXAFS) spectra were collected at the U-L_3 absorption edge at the XAS Beamline (Australian Synchrotron). Spectra were collected for eight powdered core samples (MR5076a, MR5076b, MR5077, MR5613a, MR5613b, MR5766b, MR5766c, MR5766d,) selected because they had sufficient U concentrations (from ICP-MS results) to yield good quality spectra, and nine U-bearing minerals provided by the Melbourne Museum serving as standards. Data on these standards are presented in the supplementary information (**Error! Reference source not found.**, SI Figure 2 and SI Figure 3). Homogenised powdered samples or mineral standards diluted with boron nitride were packed into Al holders, and sealed with Kapton tape. For analysis, samples were loaded into a He cryostat (pulse-tube Optistat, Oxford Instruments; T~10K). In addition, spectra were taken from a fresh section of the core subsample CD 1577 at six random points. The incident energy was controlled using a Si(111) double crystal monochronomator and calibrated at the Zr-K absorption edge using a Zr metal foil (first maximum of the first derivative at 17998 eV). Repeat measurements of this Zr foil established that there was no measurable energy shift during the experiments. Uranium was detected concurrently in fluorescence (100 element *Canberra* HP-Ge fluorescence detector) and transmission modes using ion chambers (*Oken*, N_2 flow at ~0.3 L/min, U = 2.1 kV). Aluminium foil was used to reduce parasitic fluorescence count rate from other fluorescence. Radiation induced changes to U valence or chemistry, assessed over repeat XANES runs, were negligible. The XANES scans were acquired as follows: baseline,

17010 to 17141 eV in 3 eV steps; over the edge-step, 17144 to 17204 eV in 0.3 eV steps; and with constant steps in k-space (δk = 0.035 $Å^{-1}$) above the edge. For EXAFS measurements the energy range was extended to ~18140 eV (k~16 A^{-1}).

Spectra normalisation and linear combination fitting (LCF) were performed using the DEMETER software package (Ravel and Newville, 2005). Most spectra were truncated after 17969 eV (14 $Å^{-1}$) to avoid interference from the Zr K edge. The LCF was performed using two reference spectra, synthetic uraninite for U(IV) (Tsarev et al., 2016) and uranopilite for U(VI) (see also SI Figure 2). The uranium oxidation state was determined from the LCF data.

The EXAFS data were processed and refined using the HORAE package (Ravel and Newville, 2005) with the theoretical standards calculated by FEFF9 (Rehr et al., 2010). The k^n-weighted data (n = 1, 2, 3) were refined in *R* space. The amplitude-reduction factor (S_0^2) was estimated to be 0.85 by fitting $UO_2(NO_3)_2 \bullet 6H_2O$ (structure confirmed by powder XRD; SI Table 3 and **Error! Reference source not found.**); this value was used in the refinement of all the sample data.

4 Results

4.1 Core geochemistry

Core sample appearance varied from sandy and dry, to dark, peaty and moist, with a mean moisture content of ~12 wt. % (range 0.3 to 38 wt. %). Mean sample pH was 4.5 (range 3.5 to 7). The physicochemical data are presented in SI Table 4. The TOC concentrations of the samples averaged 22.5 wt. % (range 1 to 59 wt. %), reflecting substantial vertical *in situ* variation in the MR deposit. Samples LOI_{550} ranged from 1 to 57 wt. %, and correlated with TOC (R^2= 0.922, slope = 1.04, $p < 0.005$; n = 10). Further LOI performed at 900 ^oC (LOI_{900})

ranged from 1 to 78.3 wt. % (average = 31 wt. %). This mass loss between 550 and 900 ^{o}C can be attributed to decomposition of inorganic carbonates (Dean, 1974; Heiri et al., 2001).

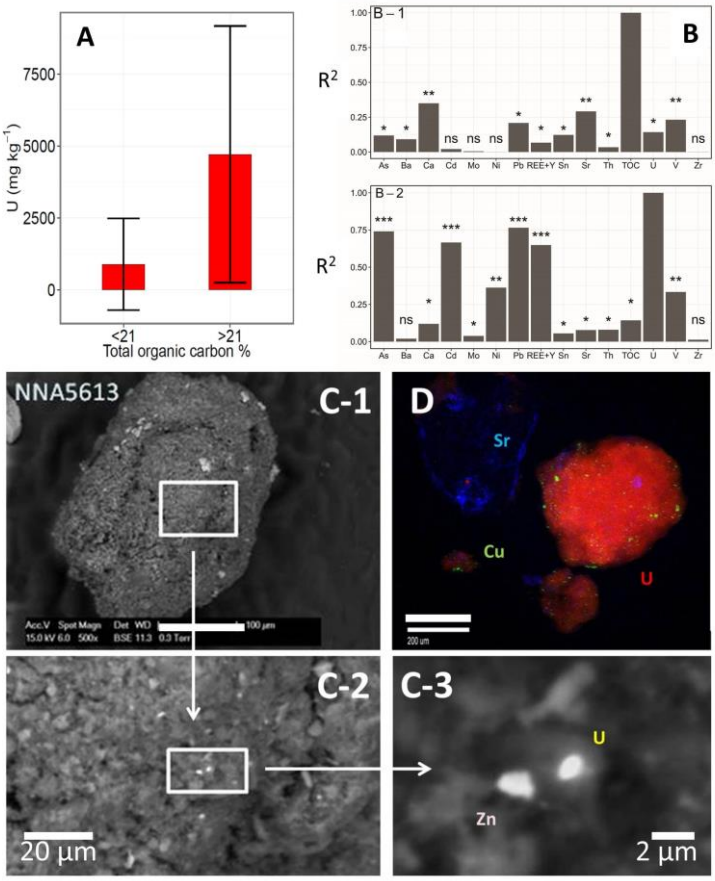

Figure 2. Uranium distribution and correlations with organic matter and trace elements. (**A**) Bar chart showing uranium distribution in samples according to carbon content. The data (n = 18) are split on the basis of their carbon contents (TOC) into two equal groups (n = 9 for each group); one group has < 21 wt. % TOC, the other 22-60 wt. % TOC. Error bars are standard deviations of uranium concentration: samples containing < 21% TOC contain 1600 mg U kg^{-1} and those with 22-60 wt. % TOC 4500 mg U kg^{-1}. (**B**) Pearson correlation coefficients for all core samples (n = 18); (**B-1**) between TOC and metals; and (**B-2**) U and metals, where height of bar corresponds to R^2 values. Stars indicate statistical significance: *** $p < 0.005$; ** $p < 0.05$; * $p < 0.5$, ns (no star) $p > 0.51$. Note that Fe was not analysed in these samples. (**C and D**) Detail of sediment grains from the MR core NNA 5613: (**C-1**) Scanning Electron Microscope (SEM) image; (**C-2**) is enlargement of (**C-1**), showing U-rich and Zn-rich particles of similar sizes. (**D**) Synchrotron x-ray fluorescence (XFM) image showing U, Cu and Sr distribution in representative grain from the same sample as (**C**); U = red, Cu = green and Sr = blue.

[full colour figure in print]

281 Uranium in the core samples ranged from 2 to 15,000 mg kg^{-1} U (mean = 2800 mg kg^{-1}, n =
282 18), and correlated with chemical digests performed on ashed samples (900 ^{o}C, n = 12)
283 when normalised to mg kg^{-1} dry mass (R^2 = 0.998, slope = 1.00, $p < 0.0005$; Pearson) (see SI
284 Table 5). Core samples contained average element concentrations in the order
285 Ti>U>Zn>Ca>total REE>Cu>Ni>Pb>Cr>Co>Sc>V>As>Th (SI Table 6). Correlations between U
286 and TOC, and U and other metals were weak ($p < 0.5$), with the strongest relationships
287 occurring between U and Pb, U and total REEs, Cd and As ($p < 0.005$, R^2 values shown in
288 Figure 2B and SI Table 7). Slight correlations were observed between TOC and Ca, Sr or V (p
289 < 0.05), but most elements show no significant correlation with TOC. Detailed analyses on
290 the organic chemistry of samples from the Mulga Rock deposit are presented elsewhere
291 (Jaraula et al 2015).

292 The spatial distribution of U in the core samples was highly variable, with U present either in
293 diffuse form (no identifiable minerals > 10 nm) or as U-rich micro- to nano- particles (see
294 XFM and SEM images in Figure 2 C and D). Sample MR5613a (from core NNA 5613, Figure 2
295 D), with a bulk U concentration of 5,000 mg kg^{-1}, showed substantial variation in the form
296 and distribution of U between the four subsamples scanned. Two subsamples contained
297 disseminated U, while U was present as discrete µm-sized particles in the other two. The
298 lignite sample CD 1577 was structurally more coherent than the March 2012 cores. The
299 mineral matrix consisted mainly of quartz (see **Error! Reference source not found.** for µXRD
300 analysis). SEM elemental mapping and BSE imaging (Figures 3, 4 and SI Figure 4 for EDS
301 spectrum) show that U exists in particulate form (µm-sized), but also forms large (up to
302 >1 mm) aggregates around Fe-sulfide minerals. The U-pyrite association is common at MR
303 (Douglas et al., (2011) as well as in many sandstone-hosted U deposits (e.g., Bonnetti et al.

(2015; 2017); Wülser et al., (2011)), and probably reflects an association between bacterial sulphate reduction and U reduction (Bonnetti et al., 2017). Micro-XRD data confirm the predominance of pyrite, and show that the main U-phase surrounding the pyrite grains/aggregates is coffinite [$USiO_4$] (**Error! Reference source not found.**). The MR coffinite has unit cell parameters (a = b = 6.943(2) Å; c = 6.262(2) Å; V = 301.9(3) Å^3) that are close to those of the Tertiary sandstone hosted Beverly deposit in South Australia (a = b = 6.971(2) Å; c = 6.255(2) Å; V = 304.0(3) Å^3; Wülser et al. (2011)).

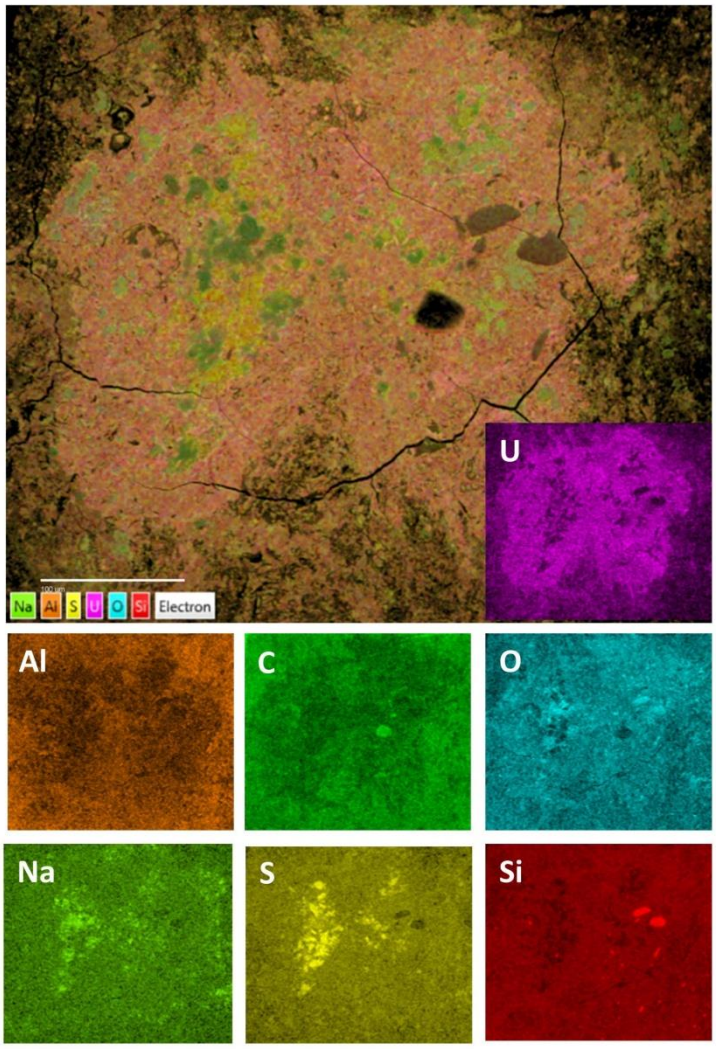

Figure 3**.** Chemical maps (U, Al, C, O, Na, S and Si) based on SEM-Energy Dispersive Spectrometry (EDS) of lignite sample CD 1577. Elemental concentrations are represented by intensity, where bright colours show high concentrations and dark or black areas represent areas where elements are absent or at low concentrations. Sulfur corresponds to pyrite

distribution. Si is associated with U (coffinite according to XRD results), bright spots correspond to quartz. Scale bar is 100 µm.
[full colour figure in print]

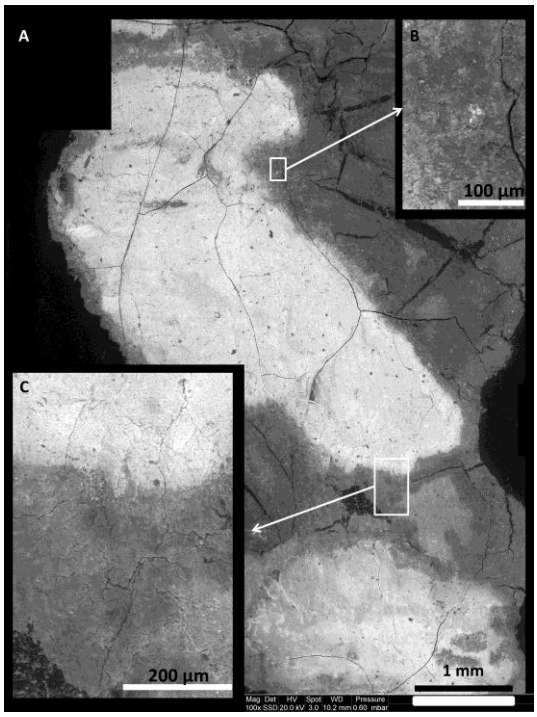

Figure 4**.** Composite ESEM backscatter image, showing distribution of uranium in the lignite section from core CD 1577. Uranium is present throughout the whole sample with the brightest phase illustrating the highest U concentration. The EXAFS spectra were taken at random points which showed that U was present in both U(IV) and U(VI) oxidation states across the sample. Inserts (B) and (C) are enlargements of indicated areas in (A).

4.2 Leach tests and XANES linear combination fits

In all samples analysed, U was present in both U(IV) and U(VI) oxidation states, with usually more U(VI) than U(IV). Bicarbonate extraction of U (U_{CO3}), a process conducted under anaerobic (N_2) conditions which targets leachable U(VI) ions, indicated that an average of 69% (SD = ±18, n = 18) of total U is in the U(VI) form. The oxidation state of U (U(IV) or U(VI)) and total concentrations of U are highly correlated (R^2 = 0.996, $p < 0.005$) with the percentage of U(VI) increasing with total U concentration, giving a slope of 0.79 for U(VI) versus total U (Figure 5A). Figure 5B shows that samples with low TOC (<8%) have a highly variable oxidation state, whereas samples with high TOC (i.e. > 20%) tend to have a

relatively constant oxidation state, dominated by U(VI) (75±7% U(VI)). Interestingly, extractions using only deionised (ultra-pure, 18.2 MΩ) water under the same anaerobic conditions as bi-carbonate method, only removed 2.5 % of the total U, showing that the majority of U was not readily water-soluble.

The U oxidation state (U_{XAS}) was independently derived from the LCF results as described above (see also **Error! Reference source not found.** and Figure 5 C and D for the normalized XANES spectra). The LCF data (**Error! Reference source not found.**) show that the uranium is predominately present (i.e. 74 %) in the higher oxidation state, +6. These results are consistent with the concentration values from CO_3-extraction. Comparison of XAS (74%) and bi-carbonate extraction datasets (69%) showed good agreement, giving an overall mean across the two methods of 71% U(VI).

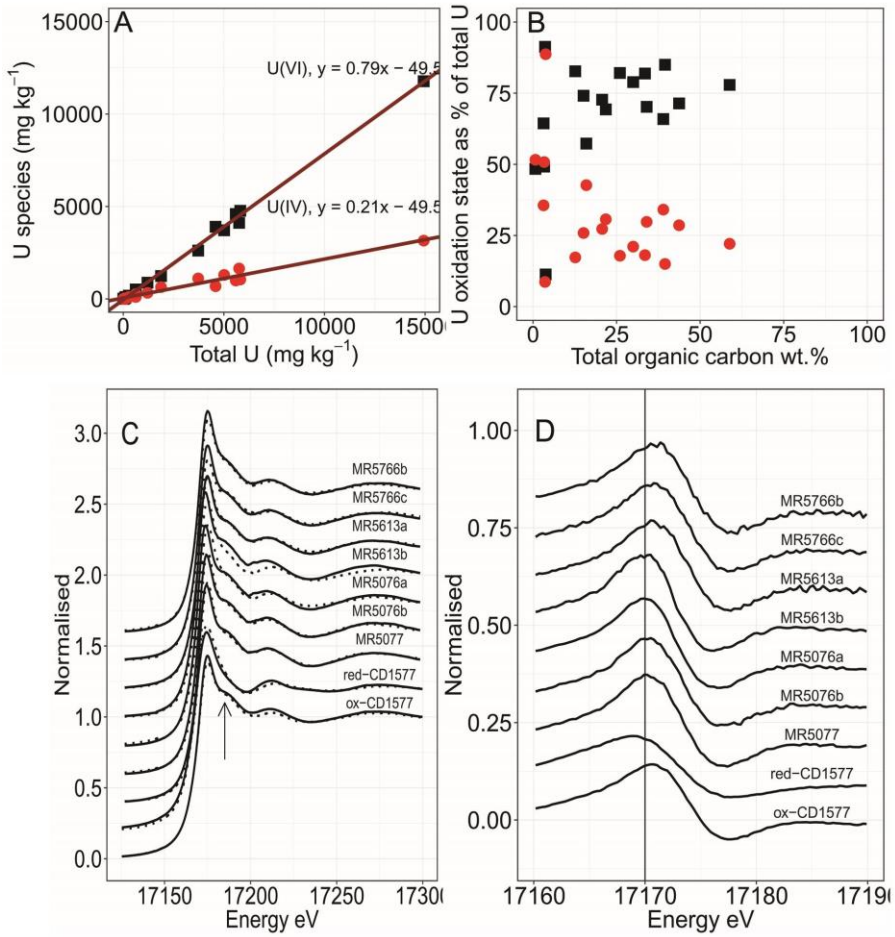

348

349 **Figure** 5. Uranium speciation as derived from bicarbonate extraction (A and B); and
350 synchrotron-XANES analyses (C and D). (**A**) Bi-carbonate extracted U(VI) and U(IV) data in
351 mg kg^{-1} (y axis) plotted as a function of total U (mg kg^{-1}). Black squares are U(VI) (R^2 = 0.996.
352 y = 0.7896x – 49.5 for U(VI)) and red dots are U(IV) (R^2 =0.21 x 49.5). **(B)** U(IV) and U(VI)
353 oxidation states as percent of total U (U(VI)/(U(VI)+U(IV)) x 100 plotted as a function of TOC
354 wt. %. Black squares =U(VI) ,and red dots =U(IV). (**C)** XAS-XANES spectra of MR bulk core
355 samples and the lignite sample CD1577. The overlain dotted line is the fitted spectra from
356 LCF The arrow marks the position of the O=U=O U(VI) shoulder. **(D)** are the derivatives of
357 **(C).**

358

359 ## 4.3 EXAFS fits

360 Two types of XANES spectra were obtained from six measurements performed on the lignite

361 sample CD 1577 (Figure 4). These spectra were grouped, merged and analysed separately,

362 with one type showing a uranyl-like (‘oxidised-CD1577’) spectrum and the other a reduced

('reduced-CD1577) U spectrum (Figure 6). The EXAFS data also differ greatly among the two types (Figure 6), and different fitting strategies were used for each type. EXAFS data from the samples MR5766c and MR5613a are similar to the 'oxidised-CD1577' lignite spectra, and were refined simultaneously.

4.3.1 Fitting of the EXAFS spectra with uranyl-like XANES

EXAFS spectra from MR5766c, MR5613a and 'oxidised-CD1577' were analysed with a common E_0, using selected paths from the uranopilite structure (amcsd 0005730; Burns (2001)), and one uranium-carbon single-scattering path from the structure of $C_{15}H_{10}O_8U$ from de Lill and Chan (2013). The advantage of this approach is that the 'oxidised-CD1577' spectra could be fitted by constraining the distances and Debye-Waller factors to be the same as those for MR5766c. To obtain the best fit for the 'oxidised-CD1577' spectra, the number of oxygen atoms (O15 only) was refined, allowing additional oxygen to be fitted that was not present in the MR5766c and MR5613a spectra. Note that the choice of C rather than another light element (e.g. O, N, P) cannot be justified by EXAFS alone. Carbon was chosen because the refined bond-distance and coordination are consistent with previous studies (see below); SEM did not reveal a correlation between U and P, or any of the poorly soluble uranyl phosphates minerals; and the samples are rich in C but poor in N (C/N≥100; Jaraula et al. 2015). The final results are shown in Table 1.

Two models were used for comparison: a simple model where the two equally short U-O distances (uranyl ion) were constrained to be the same (Table 1); and a second model where the two short U-O distances were refined independently (SI Table 9). While more complex multiple scattering (MS) paths ($U\text{-}O_{ax2}\text{-}U\text{-}O_{ax2}$, $U\text{-}O_{ax2}\text{-}O_{ax1}$ and $U\text{-}O_{ax2}\text{-}U\text{-}O_{ax1}$) could be employed to fit the data out to a distance of 3.58 Å in the second model, the two short U-O

386 bonds were the same within error (1.75(3) and 1.77(3) Å). Furthermore, the goodness-of-fit
387 parameters for both models were effectively identical, indicating that there was no
388 significant advantage to the second model, so that the simpler model (Table 1) is preferred.

389 In all cases, the fit resulted in two carbon atoms at distances of 2.90(7) to 2.93(3) Å. This
390 configuration suggests a bidentate coordination to functional groups of the solid OM. All
391 U(VI)-dominant spectra lacked a peak at distance of 3.8 Å, which would indicate the
392 presence of U-U bonds. This shows that most U is not present in the form of uranyl
393 minerals. Consequently, the most U(VI) in the studied samples is present predominantly as a
394 monomeric U(VI) complex bound to OM. This is further supported by the flattening of the
395 oscillation between 6.8 and 7.9 $Å^{-1}$ in the k^2-weighted EXAFS data (arrow, Figure 6A), a
396 feature which appears in uranyl-humic compounds (Denecke et al., 1998a; Denecke et al.,
397 1998b; Mikutta et al., 2016).

398

Table 1 Fitting parameters obtained from U L_3-Edge of EXAFS Spectra.

sample	ligand	N	R (A)	ss (A^2)	fraction	N_{tot} = N*fraction	ΔE_0	red X^2	r-factor	k-range ($Å^{-1}$)	R-range (A)	k-weighting	$S0^2$
	Oax2	2	1.773(5)	0.003 (fix)			9.2(5)	113	0.023	2 - 12	1.3 - 4	1,2,3	0.85
MR5766c	O15	2	2.22(1)	0.003 (fix)									
	O14	2	2.36(1)	0.003 (fix)									
	OH20	2	2.42(2)	0.003 (fix)									
	C	2	2.93(3)	0.003 (fix)									
	U-Oax2-U-Oax2 (MS)		3.545(7)	0.006 (fix)									
	Oax2	2	1.77(2)	0.003 (fix)			11(3)	113		3 - 11.5	1.3 - 4	1,2,3	0.85
MR5613a	O15	2	2.24(4)	0.003 (fix)									
	O14	2	2.39(4)	0.003 (fix)									
	OH20	2	2.45(6)	0.003 (fix)									
	C	2	2.90(7)	0.003 (fix)									
	U-Oax2-U-Oax2 (MS)		3.55(3)	0.006 (fix)									
oxidised-CD1577*	Oax2	2.3(2)	1.773(5)	0.003 (fix)			9(1)	113		2.5 - 12	1 - 4	1,2,3	0.85
	O15	2.8(4)	2.22(1)	0.003 (fix)									
	O14	2	2.36(1)	0.003 (fix)									
	OH20	2	2.41(2)	0.003 (fix)									
	C	**2**	**2.91(4)**	**0.003 (fix)**									
	U-Oax2-U-Oax2 (MS)		3.545(7)	0.006 (fix)									
Reduced-CD1577	Oax2	2**	1.74(2)	0.003 (fix)	0.47(10)	0.94	8(3)	199		3 – 10.5	1 - 4	1,2,3	0.85
	O15	2**	2.35(7)	0.003 (fix)	0.47(10)	0.94							
	O14	2**	2.33 (fix)	0.003 (fix)	0.47(10)	0.94							
	OH20	2**	2.37 (fix)			0.94							
	O1 (coffinite)	2**	2.25(3)	0.003 (fix)	0.53(10)	1.06							
	O2 (coffinite)	4**	2.83(3)	0.003 (fix)	0.53(10)	2.12							
	U1 (coffinite)	4**	3.79(4)	0.005(4)	0.53(10)	2.12							

* These distances were constrained to be the same as those of MR5766c and were fitted together.

** The number of ligands was fixed, the fraction of each mineral component was refined.

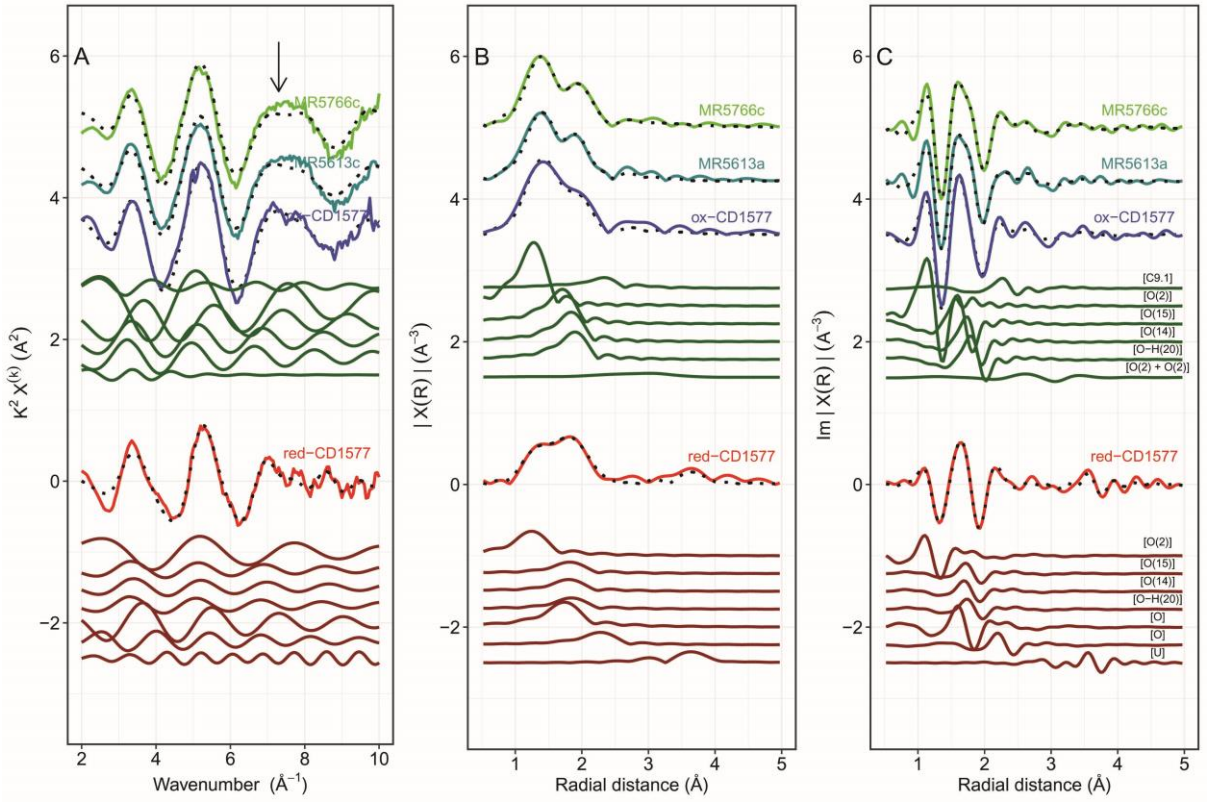

Figure 6 EXAFS data and fits, shown in (**A**) k-space; (**B**) R–space; (**C**) R- Imaginary. The uranyl-like spectra are shown at the top of each graph for MR5766c, MR5613a and CD1577 oxidised spectra (ox-MR) with relevant paths shown below. The reduced spectra (red-MR) from CD1577 is shown below in Red and relevant paths underneath.

4.3.2 Fitting of the reduced-CD1577 EXAFS spectra

The spectrum of the reduced component from the lignite (reduced-MR, CD 1577) was fitted using a wide variety of models. We report here a simple model (SI Table 3) based on a combination of paths corresponding to uranopilite [$(UO_2)_6(SO_4)O_2(OH)_6(H_2O)6{\cdot}8H_2O$], as a proxy for the uranyl component (amcsd 0005730; (Burns, 2001); and coffinite [$USiO_4$] (icsd 15484; (Fuchs and Gebert, 1958), which is the main U mineral according to micro-XRD (SI Figure 1). The best fit was obtained using 47(10) % uranopilite and 53(9.8) % coffinite. The presence of atoms at ~3.8 Å distance indicates a second shell of U consistent with the crystal structure of coffinite (EXAFS fit U-U distance of 3.79(4); crystallographic distance of 3.83(2) Å). Furthermore, Bhattacharyya et al. (2017) report a U-C distance of 2.90 Å for their

organic U(IV) structure, but this contribution is absent from the reduced-MR sample. Thus, in contrast to U(VI), which is present in mostly monomeric form within the organic matrix, U(IV) is present in mineral form (predominantly coffinite in CD 1577).

5 Discussion

5.1 U-OM association at MR

Accumulation of U by OM by 10's of 1000's of times relative to U-concentrations in groundwater is a common and long established feature. Analyses of groundwater by Douglas et al. (2011) show that modern waters at MR contain ppb concentrations of U (8 µg L^{-1}), hence implying concentrations of up to > 6 orders of magnitude in the OM layers (mean = 2500 mg kg^{-1} U, max = 15,000 mg kg^{-1} U). The highest concentrations of U at MR were associated with high concentrations of organic carbon, with 84% of the total U in half the sample set (n=9) containing >22-60 wt. % TOC. According to Douglas et al. (2011), uranium and the associated metals precipitated syngenetically with OM as it was deposited during a humid phase in the Late Eocene. Subsequent small-scale mobilisation during diagenesis and/or weathering concentrated the metals in the upper 2 m of the lignite, with the latest episode in the last 300,000 years. Continuous upgrading via interaction with groundwater containing low concentrations of dissolved U could also have contributed to the high grades observed today.

A characteristic of the OM-rich layers is that the proportion of U(VI) is relatively consistent (e.g. 77.2% ± 18 from extractions), despite the fact that absolute U concentrations vary greatly. Correlation coefficients between U and OM in soils and sediments in the literature are highly variable (Meunier et al., 1989; Landais, 1996; Min et al., 2000; Regenspurg et al.,

441 2010; Cumberland et al., 2016; Och et al., 2016) and Mulga Rock is no exception. At MR the
442 OM-rich samples contained most of the U identified across all the studied samples, yet no
443 statistically significant correlation existed between grade and OM content. We infer that U
444 introduced in oxidized form (uranyl complexes) by groundwater flowing through the OM-
445 rich sediments sorbed strongly and immediately to the available sites on the organic carbon.

446 We examined MR samples for U oxidation state, as this parameter controls the potential for
447 U mobility and biotoxicity, as well as providing necessary data to inform design of the ore-
448 forming process. The results of both XAS and HCO_3^--chemical extractions show that on
449 average 71% of the total U (mean of 69% HCO_3 extraction and 74% XAS LCF) was in the U(VI)
450 oxidation state in the MR samples. That most of the U was observed as U(VI) was surprising
451 given the long-held assumption that for long-term U immobilisation and accumulation to
452 occur within OM-rich sediments, reduction would be more important than adsorption
453 (Spirakis, 1996). In the case of MR specifically, the presence of high proportions of reduced
454 U might also have been expected, given the low to neutral pH (3.5 to 7), reducing
455 conditions, and abundant coffinite/uraninite particles within the ores (Douglas et al., 2011).
456 However, while U phase stability modelling at low pH and Eh predicts that uraninite (UO_2)
457 and coffinite (under quartz-supersaturation conditions; Brugger et al., (2005)) are the
458 dominant phases in the absence of OM (Langmuir, 1978), models that include OM as
459 humate suggest a U(VI)-humate phase dominating at ~pH 6 (Shanbhag and Choppin, 1981;
460 Lenhart et al., 1997; Cumberland et al., 2016).

461 Recent studies have shown that modern OM-rich soils contain a high proportion of U(VI) (32
462 -65 % U(VI) in peats, and 51 to 100 % U(VI) in organic-rich alpine soils; (Regenspurg et al.,
463 2010; Mikutta et al., 2016). Hence, the predominance of U(VI) at MR might be explained by

short U residence times and slow reduction kinetics. However, Jaraula et al. (2015) showed that U has been present at MR long enough to cause radiolytic damage to organic biomarkers. We therefore interpret that since the first sediments were deposited, U(VI) reduction has not played a major role in immobilizing U, despite the fact that MR is a shallow (<50 m) deposit undergoing deep weathering, and has remained in contact with groundwater containing μg L^{-1} levels of U. Furthermore, the ores exist in an environment where both inorganic and microbial redox processes are expected to be promoted – as indeed demonstrated locally by the abundance of biogenic sulphide minerals.

5.2 Uranium - organic matter complexes

The poor capability of pure water to extract U compared to the bicarbonate leach (2.5% versus 69% extraction) suggests poor U(VI) solubility and strong U(VI) association to particulate OM (i.e. > 1.2 μm filter-size) or possibly finely dispersed silica. We therefore postulate that particulate OM has helped to retard U mobility at MR, especially since only very low concentrations of U persisted within neighbouring sandstone sediments that were lower in organic carbon.

Mikutta et al. (2016) reported that uranyl present in modern peats (e.g. <13,000 years) is surrounded by 0.9 to 2.0 carbons at 2.89-2.93 Å. Therefore the speciation in the MR lignite, where we identified a bidentate C coordination at similar distance (2.90(7) to 2.93(3) Å) appears to be surprisingly similar to that in modern peat. This U-carbon model is also consistent with that of Denecke et al. (1998a; 1998b), representing poorly-ordered UO_2^{2+} bonding to $COOH^-$ (carboxylic acid) groups present in organic macromolecules (Kaplan et al., 2016). Such bonding is likely at MR, considering that Douglas et al. (2011) found that up to 13.1% of the carbon is present in carboxyl groups within the MR OM-rich sediments.

Bhattacharyya et al. (2017) showed that uranium could remain attached to these carboxyl ligands even if U was reduced *in situ* to U(IV); however at MR, U reduction appears to be mainly associated with the formation of coffinite and/or uraninite particles.

6 Conclusion

Our findings show that uranium at Mulga Rock was mostly (85%) associated with the organic-rich sediments, where most of it is present in the oxidised state of U(VI) (71% of total U). It is commonly assumed that the flow of groundwater largely determines the distribution of the U; however, this study found that U was associated with higher organic matter concentrations, and therefore the mobility of U can be inhibited by OM. Results from EXAFS analyses on the oxidised CD1577 spectra are consistent with the interpretation that uranium predominantly forms a bidendate U(VI) complex with two organic (likely carboxyl) groups.

Despite the dominant presence of OM, U(VI) was found to be reduced only incompletely, even under low pH conditions. Hence, MR-OM itself did not readily reduce U, and reduction of U was not required for immobilisation of uranium over geological time frames as applicable to Mulga Rock. Tetravalent U, which displayed consistency with a coffinite–like structure, was found to be widely present at Mulga Rock; these species most likely result from *in situ* U(VI) reduction as a consequence of heterogeneous secondary processes, such as biomediated sulfate reduction and pyrite mineralisation and/or microbial enzymatic activity.

Our results extend a growing body of evidence that U speciation in OM-rich geological materials involves a complex mixture of U(IV) and U(VI), representing potentially

overprinting generations of U delivery by groundwater and subsequent biologically-mediated U(VI) reduction. These results have direct implications for the development of U-OM chemical extraction methods and post-mining management practices: In the context of in-situ recovery, oxidation is not necessarily required for mobilising U, as U(VI) is present in higher proportions than previously assumed. In the case of remediation, environmental management strategies can shift from a focus on U reduction to using OM to capture U in its uranyl form, as a potentially equally effective or preliminary approach to U remediation. Future research into different forms of environmental U-OM interactions, in the presence of other potentially reactive components such as mineral surfaces and microorganisms, is necessary, to understand the conditions under which U can be released or immobilised in OM-rich waters and sediments.

7 Acknowledgements

This work was funded through a grant to JWM from the CSIRO Organic Geochemistry of Mineral Systems (OGMS) Research Cluster. Parts of this research were undertaken on the XAS and XFM beamline at the Australian Synchrotron, part of ANSTO. We would like to thank: Xavier Moreau (Vimy Resources) for MR samples; Dr Alan Grieg, Graham Hutchinson and Dr Hong Vu for laboratory assistance; Prof. Lorenz Schwark (University of Kiel) for TOC, N and S data analysis; Dr Martin De Jonge and Dr Daryl Howard for beamline assistance at AS XFM, Museum Victoria for comparative minerals, and Steven Henderson for his editorial contributions. SC would like to thank the Australian Synchrotron (AS) for beamtime and the AS and Monash University for support in preparation of this manuscript through a joint post-doctoral fellowship.

8 References

Alessi, D.S., Uster, B., Veeramani, H., Suvorova, E.I., Lezama-Pacheco, J.S., Stubbs, J.E., Bargar, J.R., Bernier-Latmani, R., 2012. Quantitative Separation of Monomeric U(IV) from UO2 in Products of U(VI) Reduction. Environmental Science & Technology 46, 6150-6157, doi:10.1021/es204123z.

Bargar, J.R., Williams, K.H., Campbell, K.M., Long, P.E., Stubbs, J.E., Suvorova, E.I., Lezama-Pacheco, J.S., Alessi, D.S., Stylo, M., Webb, S.M., Davis, J.A., Giammar, D.E., Blue, L.Y., Bernier-Latmani, R., 2013. Uranium redox transition pathways in acetate-amended sediments. Proceedings of the National Academy of Sciences 110, 4506-4511, doi:10.1073/pnas.1219198110.

Bhattacharyya, A., Campbell, K.M., Kelly, S.D., Roebbert, Y., Weyer, S., Bernier-Latmani, R., Borch, T., 2017. Biogenic non-crystalline U(IV) revealed as major component in uranium ore deposits. Nature Communications 8, 15538, doi:10.1038/ncomms15538.

Bone, S.E., Dynes, J.J., Cliff, J., Bargar, J.R., 2017. Uranium(IV) adsorption by natural organic matter in anoxic sediments. Proceedings of the National Academy of Sciences 114, 711–716, doi:10.1073/pnas.1611918114.

Bonnetti, C., Cuney, M., Michels, R., Truche, L., Malartre, F., Liu, X., Yang, J., 2015. The Multiple Roles of Sulfate-Reducing Bacteria and Fe-Ti Oxides in the Genesis of the Bayinwula Roll Front-Type Uranium Deposit, Erlian Basin, NE China. Economic Geology 110, 1059-1081.

Bonnetti, C., Liu, X., Zhaobin, Y., Cuney, M., Michels, R., Malartre, F., Mercadier, J., Cai, J., 2017. Coupled uranium mineralisation and bacterial sulphate reduction for the genesis of the Baxingtu sandstone-hosted U deposit, SW Songliao Basin, NE China. Ore Geology Reviews 82, 108-129, doi:10.1016/j.oregeorev.2016.11.013.

Brugger, J., Long, N., McPhail, D.C., Plimer, I., 2005. An active amagmatic hydrothermal system: The Paralana hot springs, Northern Flinders Ranges, South Australia. Chemical Geology 222, 35-64, doi:10.1016/j.chemgeo.2005.06.007.

Bryan, N.D., Abrahamsen, L., Evans, N., Warwick, P., Buckau, G., Weng, L., Van Riemsdijk, W.H., 2012. The effects of humic substances on the transport of radionuclides: Recent improvements in the prediction of behaviour and the understanding of mechanisms. Applied Geochemistry 27, 378-389, doi:10.1016/j.apgeochem.2011.09.008.

Burns, P.C., 2001. A new uranyl sulfate chain in the structure of uranopilite. The Canadian Mineralogist 39, 1139-1146.

Campbell, K.M., Gallegos, T.J., Landa, E.R., 2015. Biogeochemical aspects of uranium mineralization, mining, milling, and remediation. Applied Geochemistry 57, 206-235, doi:10.1016/j.apgeochem.2014.07.022.

Cumberland, S.A., Douglas, G., Grice, K., Moreau, J.W., 2016. Uranium mobility in organic matter-rich sediments: A review of geological and geochemical processes. Earth-Science Reviews 159, 160-185, doi:10.1016/j.earscirev.2016.05.010.

de Lill, D.T., Chan, B.C., 2013. Structure and luminescence of a one-dimensional uranium coordination polymer assembled through benzophenone-4,4′-dicarboxylate. Inorganica Chimica Acta 404, 215-218, doi:https://doi.org/10.1016/j.ica.2013.03.006.

Dean, W.E., 1974. Determination of carbonate and organic matter in calcareous sedimentry rocks by loss of ignition:Comparison with other methods. Journal of Sedimentary Petrology 44, 242-248, doi:doi:10.1306/74D729D2-2B21-11D7-8648000102C1865D

Deditius, A.P., Utsunomiya, S., Ewing, R.C., 2008. The chemical stability of coffinite, USiO4.*n*H(2)O; 0<n<2, associated with organic matter: A case study from Grants uranium region, New Mexico, USA. Chemical Geology 251, 33-49, doi:10.1016/j.chemgeo.2008.02.009.

Denecke, M.A., Reich, T., Bubner, M., Pompe, S., Heise, K.H., Nitsche, H., Allen, P.G., Bucher, J.J., Edelstein, N.M., Shuh, D.K., 1998a. Determination of structural parameters of uranyl ions complexed

580 with organic acids using EXAFS. Journal of Alloys and Compounds 271, 123-127, doi:10.1016/s0925-
581 8388(98)00038-3.
582 Denecke, M.A., Reich, T., Pompe, S., Bubner, M., Heise, K.H., Nitsche, H., Allen, P.G., Bucher, J.J.,
583 Edelstein, N.M., Shuh, D.K., Czerwinski, K.R., 1998b. EXAFS investigations of the interaction of humic
584 acids and model compounds with uranyl cations in solid complexes. Radiochimica Acta 82, 103-108.
585 Douglas, G.B., Butt, C.R.M., Gray, D.J., 2011. Geology, geochemistry and mineralogy of the lignite-
586 hosted Ambassador palaeochannel uranium and multi-element deposit, Gunbarrel Basin, Western
587 Australia. Mineralium Deposita 46, 761-787, doi:10.1007/s00126-011-0349-4.
588 Douglas, G.B., Gray, D.J., Butt, C.M., 1993. Geochemistry, minerology and hydrogeochemistry of the
589 Ambassador multi-element lignite deposit, Western Australia: With additional investigations on the
590 characterization of organic matter. CSIRO, Australia.
591 Eggins, S.M., Woodhead, J.D., Kinsley, L.P.J., Mortimer, G.E., Sylvester, P., McCulloch, M.T., Hergt,
592 J.M., Handler, M.R., 1997. A simple method for the precise determination of ≥ 40 trace elements in
593 geological samples by ICPMS using enriched isotope internal standardisation. Chemical Geology 134,
594 311-326, doi:https://doi.org/10.1016/S0009-2541(96)00100-3.
595 Etschmann, B.E., Ryan, C.G., Brugger, J., Kirkham, R., Hough, R.M., Moorhead, G., Siddons, D.P., De
596 Geronimo, G., Kuczewski, A., Dunn, P., Paterson, D., de Jonge, M.D., Howard, D.L., Davey, P., Jensen,
597 M., 2010. Reduced As components in highly oxidized environments: Evidence from full spectral
598 XANES imaging using the Maia massively parallel detector. American Mineralogist 95, 884-887,
599 doi:10.2138/am.2010.3469.
600 Fuchs, L.H., Gebert, E., 1958. X-Ray Studies of Synthetic Coffinite, Thorite and Uranothorites.
601 American Mineralogist 43, 243-248.
602 Greenwood, P., Brocks, J., Grice, K., Schwark, L., Jaraula, C., Dick, J., Evans, K., 2013. Organic
603 Geochemistry and Mineralogy: I. Characterisation of Organic Matter Associated with Metal Deposits.
604 Ore Geology Reviews, 1-27, doi:10.1016/j.oregeorev.2012.10.004.
605 Grenthe, I., Fuger, J., Konings, R.J.M., Lemire, R.J., Muller, A.B., Nguyen-Trung, C., Wanner, H., 2004.
606 Chemical Thermodynamics of Uranium. OECD- NEA, Paris, France.
607 Guillaumont, R., Fanghanel, T., Neck, V., Fuger, J., Palmer, D., Grenthe, I., Rand, M.H., 2003. Update
608 on the chemical thermodynamics of uranium, neptunium, plutonium, americium, and technetium.
609 OECD, Nuclear Energy Agency, Paris, France, p. 959.
610 Heiri, O., Lotter, A., Lemcke, G., 2001. Loss on ignition as a method for estimating organic and
611 carbonate content in sediments: reproducibility and comparability of results. Journal of
612 Paleolimnology 25, 101-110, doi:10.1023/a:1008119611481.
613 Idiz, E.F., Carlisle, D., Kaplan, I.R., 1986. Interaction between organic matter and trace metals in a
614 uranium rich bog, Kern County, California, U.S.A. Applied Geochemistry 1, 573-590,
615 doi:10.1016/0883-2927(86)90065-X.
616 Jaraula, C.M.B., Schwark, L., Moreau, X., Pickel, W., Bagas, L., Grice, K., 2015. Radiolytic alteration of
617 biopolymers in the Mulga Rock uranium deposit. Applied Geochemistry 52, 97-108,
618 doi:10.1016/j.apgeochem.2014.11.012.
619 Kamber, B.S., Greig, A., Schoenberg, R., Collerson, K.D., 2003. A refined solution to Earth's hidden
620 niobium: implications for evolution of continental crust and mode of core formation. Precambrian
621 Research 126, 289-308, doi:https://doi.org/10.1016/S0301-9268(03)00100-1.
622 Kanematsu, M., Perdrial, N., Um, W., Chorover, J., O'Day, P.A., 2014. Influence of Phosphate and
623 Silica on U(VI) Precipitation from Acidic and Neutralized Wastewaters. Environmental Science &
624 Technology 48, 6097-6106, doi:10.1021/es4056559.
625 Kaplan, D.I., Xu, C., Huang, S., Lin, Y., Tolić, N., Roscioli-Johnson, K.M., Santschi, P.H., Jaffé, P.R., 2016.
626 Unique Organic Matter and Microbial Properties in the Rhizosphere of a Wetland Soil.
627 Environmental Science & Technology 50, 4169-4177, doi:10.1021/acs.est.5b05165.
628 Landais, P., 1996. Organic geochemistry of sedimentary uranium ore deposits. Ore Geology Reviews
629 11, 33-51, doi:10.1016/0169-1368(95)00014-3.

Langmuir, D., 1978. Uranium solution-mineral equilibria at low temperatures with applications to sedimentary ore deposits. Geochimica et Cosmochimica Acta 42, 547-569, doi:10.1016/0016-7037(78)90001-7.
Latta, D.E., Mishra, B., Cook, R.E., Kemner, K.M., Boyanov, M.I., 2014. Stable U(IV) Complexes Form at High-Affinity Mineral Surface Sites. Environmental Science & Technology 48, 1683-1691, doi:10.1021/es4047389.
Law, G.T.W., Geissler, A., Burke, I.T., Livens, F.R., Lloyd, J.R., McBeth, J.M., Morris, K., 2011. Uranium Redox Cycling in Sediment and Biomineral Systems. Geomicrobiology Journal 28, 497-506, doi:10.1080/01490451.2010.512033.
Lenhart, J.J., Figueroa, L.A., Honeyman, B.D., Kaneko, D., 1997. Modeling the adsorption of U(VI) onto animal chitin using coupled mass transfer and surface complexation. Colloids and Surfaces A: Physicochemical and Engineering Aspects 120, 243-254, doi:10.1016/S0927-7757(96)03865-4.
Li, K., Etschmann, B., Rae, N., Reith, F., Ryan, C.G., Kirkham, R., Howard, D., Rosa, D.R.N., Zammit, C., Pring, A., Ngothai, Y., Hooker, A., Brugger, J., 2016. Ore Petrography Using Megapixel X-Ray Imaging: Rapid Insights into Element Distribution and Mobilization in Complex Pt and U-Ge-Cu Ores. Economic Geology 111, 487-501, doi:10.2113/econgeo.111.2.487.
Lidman, F., Mörth, C.M., Laudon, H., 2012. Landscape control of uranium and thorium in boreal streams – spatiotemporal variability and the role of wetlands. Biogeosciences 9, 4773-4785, doi:10.5194/bg-9-4773-2012.
Luo, W., Gu, B., 2008. Dissolution and Mobilization of Uranium in a Reduced Sediment by Natural Humic Substances under Anaerobic Conditions. Environmental Science & Technology 43, 152-156, doi:10.1021/es8013979.
Mehta, V.S., Maillot, F., Wang, Z., Catalano, J.G., Giammar, D.E., 2014. Effect of co-solutes on the products and solubility of uranium(VI) precipitated with phosphate. Chemical Geology 364, 66-75, doi:10.1016/j.chemgeo.2013.12.002.
Meunier, J.D., Trouiller, A., Brulhert, J., Pagel, M., 1989. Uranium and organic matter in a paleodeltaic environment; the Coutras Deposit (Gironde, France). Economic Geology 84, 1541-1556.
Mikutta, C., Langner, P., Bargar, J.R., Kretzschmar, R., 2016. Tetra- and Hexavalent Uranium Forms Bidentate-Mononuclear Complexes with Particulate Organic Matter in a Naturally Uranium-Enriched Peatland. Environmental Science & Technology 50, 10465–10475, doi:10.1021/acs.est.6b03688.
Min, M.Z., Meng, Z.W., Sheng, G.Y., Min, Y.S., Liu, X., 2000. Organic geochemistry of paleokarst-hosted uranium deposits, South China. Journal of Geochemical Exploration 68, 211-229, doi:10.1016/s0375-6742(99)00085-0.
Newsome, L., Morris, K., Lloyd, J.R., 2014. The biogeochemistry and bioremediation of uranium and other priority radionuclides. Chemical Geology 363, 164-184, doi:10.1016/j.chemgeo.2013.10.034.
Och, L.M., Müller, B., März, C., Wichser, A., Vologina, E.G., Sturm, M., 2016. Elevated uranium concentrations in Lake Baikal sediments: Burial and early diagenesis. Chemical Geology 441, 92-105, doi:10.1016/j.chemgeo.2016.08.001.
Owen, D.E., Otton, J.K., 1995. Mountain wetlands: Efficient uranium filters — potential impacts. Ecological Engineering 5, 77-93, doi:10.1016/0925-8574(95)00013-9.
Paterson, D., de Jonge, M.D., Howard, D.L., Lewis, W., McKinlay, J., Starritt, A., Kusel, M., Ryan, C.G., Kirkham, R., Moorhead, G., Siddons, D.P., 2011. The X-ray Fluorescence Microscopy Beamline at the Australian Synchrotron. In: McNulty, I., Eyberger, C., Lai, B. (Eds.). 10th International Conference on X-Ray Microscopy, pp. 219-222.
Ravel, B., Newville, M., 2005. ATHENA, ARTEMIS, HEPHAESTUS: data analysis for X-ray absorption spectroscopy using IFEFFIT. Journal of Synchrotron Radiation 12, 537-541, doi:10.1107/s0909049505012719.
Read, D., Bennett, D.G., Hooker, P.J., Ivanovich, M., Longworth, G., Milodowski, A.E., Noy, D.J., 1993. The migration of uranium into peat-rich soils at Broubster, Caithness, Scotland, U.K. Journal Of Contaminant Hydrology 13, 291-308, doi:10.1016/0169-7722(93)90067-3.

Regenspurg, S., Margot-Roquier, C., Harfouche, M., Froidevaux, P., Steinmann, P., Junier, P., Bernier-Latmani, R., 2010. Speciation of naturally-accumulated uranium in an organic-rich soil of an alpine region (Switzerland). Geochimica et Cosmochimica Acta 74, 2082-2098, doi:10.1016/j.gca.2010.01.007.

Rehr, J.J., Kas, J.J., Vila, F.D., Prange, M.P., Jorissen, K., 2010. Parameter-free calculations of X-ray spectra with FEFF9. Physical Chemistry Chemical Physics 12, 5503-5513, doi:10.1039/b926434e.

Renock, D., Mueller, M., Yuan, K., Ewing, R.C., Becker, U., 2013. The energetics and kinetics of uranyl reduction on pyrite, hematite, and magnetite surfaces: A powder microelectrode study. Geochimica et Cosmochimica Acta 118, 56-71, doi:10.1016/j.gca.2013.04.019.

Rowell, D.L., 1994. Soil Science Methods and Applications. Longman UK, Harlow, England.

Ryan, C., 2000. Quantitative trace element imaging using PIXE and the nuclear microprobe. International Journal of Imaging Systems and Technology 11, 219-230.

Ryan, C., Jamieson, D., 1993. Dynamic analysis: on-line quantitative PIXE microanalysis and its use in overlap-resolved elemental mapping. Nuclear Instruments and Methods in Physics Research Section B: Beam Interactions with Materials and Atoms 77, 203-214.

Ryan, C.G., Siddons, D.P., Kirkham, R., Li, Z.Y., Jonge, M.D.d., Paterson, D.J., Kuczewski, A., Howard, D.L., Dunn, P.A., Falkenberg, G., Boesenberg, U., Geronimo, G.D., Fisher, L.A., Halfpenny, A., Lintern, M.J., Lombi, E., Dyl, K.A., Jensen, M., Moorhead, G.F., Cleverley, J.S., Hough, R.M., Godel, B., Barnes, S.J., James, S.A., Spiers, K.M., Alfeld, M., Wellenreuther, G., Vukmanovic, Z., Borg, S., 2014. Maia X-ray fluorescence imaging: Capturing detail in complex natural samples. Journal of Physics: Conference Series 499, 012002.

Shanbhag, P.M., Choppin, G.R., 1981. Binding of uranyl by humic acid. Journal of Inorganic and Nuclear Chemistry 43, 3369-3372, doi:10.1016/0022-1902(81)80117-0.

Spirakis, C.S., 1996. The roles of organic matter in the formation of uranium deposits in sedimentary rocks. Ore Geology Reviews 11, 53-69, doi:10.1016/0169-1368(95)00015-1.

Tinnacher, R.M., Nico, P.S., Davis, J.A., Honeyman, B.D., 2013. Effects of Fulvic Acid on Uranium(VI) Sorption Kinetics. Environmental Science & Technology 47, 6214-6222, doi:10.1021/es304677c.

Tokunaga, T.K., Kim, Y., Wan, J., Yang, L., 2012. Aqueous Uranium(VI) Concentrations Controlled by Calcium Uranyl Vanadate Precipitates. Environmental Science & Technology 46, 7471-7477, doi:10.1021/es300925u.

Tokunaga, T.K., Wan, J.M., Pena, J., Brodie, E.L., Firestone, M.K., Hazen, T.C., Sutton, S.R., Lanzirotti, A., Newville, M., 2005. Uranium reduction in sediments under diffusion-limited transport of organic carbon. Environmental Science & Technology 39, 7077-7083, doi:10.1021/es050221a.

Tsarev, S., Collins, R.N., Fahy, A., Waite, T.D., 2016. Reduced Uranium Phases Produced from Anaerobic Reaction with Nanoscale Zerovalent Iron. Environmental Science & Technology 50, 2595-2601, doi:10.1021/acs.est.5b06160.

Vimy, 2014. Mulga Rock Uranium Project Resource Upgrade. Perth.

Vimy, 2015. Pre-Feasibility Study Reaffirms Mulga Rock Project as one of Australia's Leading Undeveloped Uranium Projects

Vimy, 2016a. Resource Update for Mulga Rock Project.

Vimy, 2016b. Significant Resource Upgrade for Mulga Rock Project.

Vimy, 2016c. Vimy Resources Limited; Annual Report 2016. Perth, p. 98.

Warwick, P., Evans, N., Hall, A., Walker, G., Steigleder, E., 2005. Stability constants of U(VI) and U(IV)-humic acid complexes. Journal of Radioanalytical and Nuclear Chemistry 266, 179-190, doi:10.1007/s10967-005-0890-7.

Wood, S.A., 1996. The role of humic substances in the transport and fixation of metals of economic interest (Au, Pt, Pd, U, V). Ore Geology Reviews 11, 1-31, doi:10.1016/0169-1368(95)00013-5.

Wülser, P.-A., Brugger, J., Foden, J., Pfeifer, H.-R., 2011. The Sandstone-Hosted Beverley Uranium Deposit, Lake Frome Basin, South Australia: Mineralogy, Geochemistry, and a Time-Constrained Model for Its Genesis. Economic Geology 106, 835-867, doi:10.2113/econgeo.106.5.835.

730 Zammit, C.M., Brugger, J., Southam, G., Reith, F., 2014. In situ recovery of uranium — the microbial
731 influence. Hydrometallurgy 150, 236-244, doi:10.1016/j.hydromet.2014.06.003.
732 Zhao, D., Wang, X., Yang, S., Guo, Z., Sheng, G., 2012. Impact of water quality parameters on the
733 sorption of U(VI) onto hematite. Journal of Environmental Radioactivity 103, 20-29,
734 doi:10.1016/j.jenvrad.2011.08.010.
735 Zhou, P., Gu, B.H., 2005. Extraction of oxidized and reduced forms of uranium from contaminated
736 soils: Effects of carbonate concentration and pH. Environmental Science & Technology 39, 4435-
737 4440, doi:10.1021/es0483443.
738
739
740

Characterization of uranium redox state in organic-rich Eocene sediments

Susan A Cumberland[1,2,3], Barbara Etschmann[2], Joël Brugger[2], Grant Douglas[4], Katy Evans[5], Louise Fisher[6], Peter Kappen[3], John W. Moreau[1]

1 School of Earth Sciences, University of Melbourne, Parkville, Victoria 3100, Australia

2 School of Earth, Atmosphere and Environment, Monash University, Clayton 3800, Victoria, Australia

3 ANSTO Australian Synchrotron, 800 Blackburn Road, Clayton 3168, Victoria, Australia

4 CSIRO Land and Water, Floreat, Western Australia, Australia

5 Western Australian School of Mines, Curtin University, Bentley, Western Australia, Australia

6 CSIRO Mineral Resources, Bentley, Western Australia, Australia

SUPPLEMENTARY INFORMATION

SI Table 1 Location and drill depth of cores analysed

Hole Id	Deposit	Samples from core	Northing	Easting	RL	Core Depth (m)	Type
NNA 5612	Princess	MR5612a,b	6684044.69	578834.44	342.8	54	AC
NNA 5613	Princess	MR5613a,b	6684001.28	578902.04	341.48	54	AC
NNA 5636	Princess	MR5636	6684253.49	579486.8	345.52	72	AC
NNA 5706	Emperor	MR5706a,b	6690894.00	552782.00	334.5	62	AC
NNA 5728	Shogun	MR5728a,b	6686912.00	563587.00	318.4	51.0	AC
NNA 5766	Ambassador	MR5766a,b,c,d	6682660.00	576969.00	342.1	64	AC
NND 5076	Emperor	MR5076a,b	6682834.90	579131.20	339.5	48.5	DDH
NND 5077	Ambassador	MR5077	6682189.32	576147.80	333	54.3	DDH
NND 5078	Ambassador	MR5078	6682605.99	577075.96	342.4	57.0	DDH
CD1577	Ambassador		6682708.94	579942.81	331.4	43.5	DDH

AC = air core; DDH = diamond drill hole, RL = Reduced Level – elevation above sea level in metres of the drill hole collar (Vimy, 2014, 2016b)

SI Table 2 Uranium mineral standards and location where known

Number	Name	Formula	Location
M 33701	andersonite	$Na_2CaUO_2(CO_3)_3 \cdot 6H_2O$	
M 21676	autunite	$Ca(UO_2)_2 (PO_4)_2$	
M 30851	boltwoodite	$(Na, K)(UO_2)_2(HSiO_4) \cdot H_2O$	
M 33175	brannerite	$U TiO_4$	
M 32495	coffinite	$USiO_4$	
M 28752	coffinite	$USiO_4$	USA, New Mexico Gransted, McKinley Country, Paddy Murphy Mines (35 8 50N, 107 51 3 W)
M 33214	curienite	$Pb_2(UO_2)_2(V_2O_8)_2 \cdot 5H_2O$	
M 22869	davidite	$(La, Ce)(Y, U, Fe)(Ti,Fe3+)_{20} (O,HO)_{38}$	
M 45514	saleeite	$Mg(UO_2)_2(PO_4)_2 \cdot 10H_2O$	
M 44367	schoepite	$(UO_2)O_2(OH)_{12} \cdot 12H_2O$	Democratic Republic of Congo (Zaire), Shaba (Katanga) Province, Kolwezi Munsonoi Mine (10 45 S 25 25 E)
M 17631	torbernite	$Cu(UO_2)_2(PO_4)_2 \cdot 8 - 12 H_2O$	
M 27299	soddyite	$(UO_2)SiO_4(H_2O)_2$	Democratic Republic of Congo (Zaire), Shaba (Katanga) Province, Swamba
M 26415	uraninite	UO_2	
M 19266	uraninite	UO_2	Australia, Northern Territory, South Alligator River
M 34470	uranophane	$Ca(UO_2)_2(SiO_3)(OH)_2 \cdot 5H_2O$	
M 40774	uranopilite	$(UO_2)_6 (SO_4)O_2 (OH)_6 (H_2O)_6$	
M 34904	uranopilite	$(UO_2)_6 (SO_4)O_2 (OH)_6 (H_2O)_6$	El Sherana mine, South Alligator River, NT, AU (13 31 S 132 31 E)
M 25802	zippeite	$Mg (UO_2)_6 (SO_4)_3 (OH)_{10} (H_2 O)_n$	

Source: Museum Victoria, formulas are generic

SI Table 3 EXAFS fitting and paths for the uranyl nitrate standard

Ligand	N	R (Å)	ss (Å^2)	ΔE_0	Red X^2	k-range	R-range	k-weighting	SO^2
O1	2 (fix)	1.787(7)	0.002(1)	10(1)	978	1-4.5 Å^{-1}	2-12.5 Å	1,2,3	0.85
O2	2 (fix)	2.34(3)	0.008(7)						
N1	2 (fix)	2.47(4)	0.003 (fix)						
O3	2 (fix)	2.53(3)	0.003 (fix)						
O4_2(path 37)	4 (fix)	4.30(3)	0.003 (fix)						
MS paths	21: O1-O1	3.57(1)	0.002(1)						
	22: O1-O1	3.57(1)	0.002(1)						
	24: N1-O1	3.65(4)	0.0025						
	27: O3-O1	3.71(3)	0.0025						
error (quadrature) for MS paths									
0.009899495									
0.040607881									
0.030805844									

SI Table 4 Summary of physicochemical data in MR cores n = 18.

Sample ID	Core	Depth (m)	Deposit	U (mg kg^{-1})	pH	TOC %	LOI_{550} %	LOI_{900} %	Carbonate % (**)	Total N %
CD1577	1577	43.5	Amb	nd	nd	nd	nd	nd	nd	nd
MR5076a	5076	44.3-44.4	Amb	1877	5.24	39	NA	NA	NA	0.46
MR5076b	5076	44.7-44.8	Amb	14930	3.09	30	NA	NA	NA	0.42
MR5077	5077	42.2-42.5	Amb	5760	4.12	44	NA	NA	NA	0.37
MR5078	5078	51.5-51.5	Amb	3720	3.02	34	NA	NA	NA	0.27
MR5612a	5612	41-42	Pri	2	4.7	60	57.7	78.3	17.3	0.35
MR5612b	5612	43-44	Pri	3.2	4.34	3.8	NA	NA	NA	0.04
MR5612c	5612	45-46	Pri	65	3.22	3.3	NA	NA	NA	0.05
MR5613a*	5613	40-41	Pri	5816	5.57	33.5	43.4	55.9	17.1	0.23
MR5613b*	5613	41-43	Pri	4588	5.61	39.5	NA	NA	NA	0.23
MR5636	5636	55-56	Pri	278	4.96	3.2	NA	NA	NA	0.05
MR5706a	5706	42-43	Emp	115	3.15	22	19.1	30.6	15.7	0.33
MR5706b	5706	55-56	Emp	40	7.06	0.72	1	1	0.1	0.02
MR5728a	5728	28.5-29	Sho	5590	3.33	26	37.9	41.9	5.1	0.29
MR5728b	5728	34-34.5	Sho	113	3.64	3.6	3.3	3.5	0.2	0.03
MR5766a	5766	53-53.5	Amb	5012	4.35	15.1	19.4	28.9	13	0.18
MR5766b*	5766	55.5-56	Amb	623	5.43	16	21.5	24.6	4.2	0.1
MR5766c*	5766	56.5-57	Amb	1206	4.60	21	22.5	33.2	14.6	0.14
MR5766d	5766	58-58.5	Amb	621	4.72	13	10.5	12.6	2.9	0.09
Mean				*2798*	*4.5*	*22.5*	*23.6*	*31.1*	*9*	*0.2*
Min				*1.9*	*3*	*0.7*	*1*	*1*	*0.1*	*0*
Max				*14932*	*7.1*	*58.8*	*57.7*	*78.3*	*17.3*	*0.5*
SD				*3805*	*1.1*	*16.8*	*17.9*	*23.6*	*7.1*	*0.1*
Median				*914.2*	*4.5*	*21.2*	*20.4*	*29.8*	*9.1*	*0.2*

*EXAFS Data available

**NB estimated CO_3^{2-} was calculated by LOI_{900} – LOI_{550} x MW C/ 100 (Dean, 1974; Heiri et al., 2001). Sample ID is the lab number given by Melbourne University. NA = not analysed

SI Table 5 Elemental data for cores (1/2)

Sample number	Core	Depth	Deposit	U (XRF)	U ashed	U	As	Be	Ca	Co	Cr	Cu
		m		mg kg^{-1}	mg kg^{-1}	mg kg^{-1}	mg kg^{-1}	mg kg^{-1}	mg kg^{-1}	mg kg^{-1}	mg kg^{-1}	mg kg^{-1}
MR5076a	5076	44.3-44.4	Amb	NA	ND	1880	17	16	12900	282	261	624
MR5076b	5076	44.7-44.8	Amb	NA	ND	14900	296	128	5290	4300	163	7290
MR5077	5077	42.2-42.5	Amb	NA	ND	5760	49	3	2950	142	880	458
MR5078	5078	51.5-51.5	Amb	NA	ND	3720	157	19	34	541	337	1500
MR5766a	5766	53-53.5	Amb	5280	5198.0	5010	50	20	2450	2960	535	696
MR5766b	5766	55.5-56	Amb	642	586.4	623	4	3	912	70	886	<LOD
MR5766c	5766	56.5-57	Amb	1160	1223.0	1210	4	6	1240	359	1080	<LOD
MR5766d	5766	58-58.5	Amb	686	641.2	621	2	2	266	640	1200	3390
MR5706a	5706	42-43	Emp	132	129.2	115	6	2	884	149	191	53
MR5706b	5706	55-56	Emp	28.5	21.7	40	0	0	50	7	520	8
MR5612a	5612	41-42	Pri	<LOD	5.8	2	6	3	4250	81	21	<LOD
MR5612b	5612	43-44	Pri	<LOD	ND	3	3	1	744	223	19	1
MR5612c	5612	45-46	Pri	80.5	<LOD	65	6	1	557	653	22	2
MR5613a	5613	40-41	Pri	5385.0	5614.0	5820	65	7	7000	83	2550	5120
MR5613b	5613	41-43	Pri	6296.0	<LOD	4590	128	4	4650	289	1300	5780
MR5636	5636	55-56	Pri	<LOD	ND	278	13	3	603	291	67	300
MR5728a	5728	28.5-29	Sho	903.0	5560	5590	6	1	974	0	1040	115
MR5728b	5728	34-34.5	Sho	<LOD	125.1	113	3	0	166	1	99	109

SI Table 5 Elemental data for cores (2/2)

sample number	core	depth	deposit	Ga	Li	Ni	Pb	Rb	Sc	Ti	Th	V	W	Zn	total REE+Y
		m		mg kg^{-1}	mg kg^{-1}	mg kg^{-1}	mg kg^{-1}	mg kg^{-1}	mg kg^{-1}	mg kg^{-1}	mg kg^{-1}	mg kg^{-1}	mg kg^{-1}	mg kg^{-1}	mg kg^{-1}
MR5076	5076	44.3-44.4	Amb	3	81	1250	158	1.9	192	5270	44	145	1.1	1750	6270
MR5076	5076	44.7-44.8	Amb	<LOD	13	8310	5290	2.4	1820	1850	10	312	0.6	3850	15400
MR5077	5077	42.2-42.5	Amb	5	1	172	3650	0.8	427	10300	12	144	2.2	14	642
MR5078	5078	51.5-51.5	Amb	24	17	2050	2750	8.5	459	45500	49	493	9.2	770	4910
MR5766a	5766	53-53.5	Amb	26	28	10800	379	2.4	915	24900	33	409	6.9	12800	5530
MR5766b	5766	55.5-56	Amb	4	4	241	236	0.9	46	7460	13	48	3.1	1810	525
MR5766c	5766	56.5-57	Amb	4	3	940	600	0.8	88	6080	12	66	3.1	2560	698
MR5766d	5766	58-58.5	Amb	3	6	1250	458	1.6	51	5010	20	30	2.8	2280	234
MR5706a	5706	42-43	Emp	19	22	85	63	11.8	24	4970	24	98	2.6	10	291
MR5706b	5706	55-56	Emp	1	4	24	8	0.4	8	474	1	4	2.2	29	22
MR5612a	5612	41-42	Pri	2	9	232	7	1.2	29	6620	5	195	1.6	3810	601
MR5612b	5612	43-44	Pri	2	4	365	4	0.3	15	6940	10	39	4.0	2050	191
MR5612c	5612	45-46	Pri	18	16	1370	11	4.5	12	3100	7	35	5.0	7840	147
MR5613a	5613	40-41	Pri	5	3	362	2290	1.3	825	11100	201	148	3.9	1620	1710
MR5613b	5613	41-43	Pri	4	5	614	2090	1.1	330	7820	33	143	2.0	<LOD	948
MR5636	5636	55-56	Pri	4	15	605	135	3.7	34	3550	11	30	1.5	1590	400
MR5728a	5728	28.5-29	Sho	49	6	4	465	4.0	377	8800	244	153	4.0	13	514
MR5728b	5728	34-34.5	Sho	1	2	1	6	0.4	7	1190	39	12	2.4	<LOD	15

SI Table 6 Summary of metals within deposits shown as average data in parts per million (mg kg^{-1})

Element	Mean	Min	Max	Ambassador n=8	Emperor n=2	Princess n=6	Shogun n=2
As	45.2	0.3	295.7	72.3	3	36.7	4.6
Be	12.2	0.1	128.3	24.6	0.8	3.3	0.3
Ca	2553	33.6	12950	3260	466.9	2966	569.9
Co	614.8	0.5	4300	1161	78.2	270.1	0.6
Cr	621	19.4	2552	668.8	355.7	662.7	570.1
Cu	1696	0.9	7286	2325	30.1	2241	111.8
Ga	9.6	0	48.8	8.3	10.1	6	24.8
Li	13.4	0.9	80.5	19.2	13.1	8.8	4.1
Ni	1594	0.7	10800	3128	54.5	591.1	2.5
Pb	1033	3.7	5292	1690	35.5	754.7	235.9
Rb	2.7	0.3	11.8	2.4	6.1	2	2.2
Sc	314.4	6.8	1822	500	15.7	207.3	191.9
Th	42.6	1.1	244.1	24	12.4	44.4	141.6
Ti	8934	474.3	45450	13290	2720	6516	4997
U	2798	1.9	14930	4219	77.9	1792	2853
V	139	4.1	492.7	205.7	51.1	98.1	82.7
W	3.2	0.6	9.2	3.6	2.4	3	3.2
Zn	2673	10.1	12770	3225	19.6	3382	12.8
REE+Y	2168	14.6	15390	4274	156.8	665.3	264.5

SI Table **7 Correlations between U and metals; TOC and metals**

Correlation Test	R	R^2	**p-value**	**significance**
U vs TOC	0.377	0.142	0.1225	*
U vs As	0.861	0.741	0.0000	***
U vs REE+Y	0.805	0.649	0.0001	***
U vs Ba	0.14	0.02	0.5786	ns
U vs Ca	0.345	0.119	0.1606	*
U vs Cd	0.816	0.666	0.0000	***
U vs Mo	0.195	0.038	0.4377	*
U vs Ni	0.602	0.363	0.0082	**
U vs Pb	0.875	0.765	0.0000	***
U vs Sn	0.234	0.055	0.3491	*
U vs Sr	0.278	0.077	0.2641	*
U vs Th	0.282	0.08	0.2567	*
U vs V	0.577	0.333	0.0121	**
U vs Zr	0.113	0.013	0.6548	ns
TOC vs As	0.344	0.118	0.1626	*
TOC vs REE+Y	0.258	0.067	0.3006	*
TOC vs Ba	0.302	0.091	0.2233	*
TOC vs Ca	0.591	0.35	0.0097	**
TOC vs Cd	0.145	0.021	0.5663	ns
TOC vs Mo	-0.069	0.005	0.7841	ns
TOC vs Ni	-0.01	0	0.9695	ns
TOC vs Pb	0.457	0.208	0.0568	*
TOC vs Sn	0.349	0.122	0.1552	*
TOC vs Sr	0.54	0.291	0.0208	**
TOC vs Th	0.184	0.034	0.4643	*
TOC vs V	0.481	0.231	0.0433	**
TOC vs Zr	0.021	0	0.9349	ns

*** p<0.005, ** p<0.05, * p <0.5, ns p >0.51

SI Table 8 Results from the linear combination fitting. Two end-members were represented by synthetic uraninite (U(IV)) and mineral uranopilite (U(VI))

							uraninite		Uranopilite	
Data	**Core**	**Rfactor**	**Chinu**	**chisqr**	**nvarys**	**scaleby**	**weight**	**error**	**weight**	**error**
MR5766c	NNA 5766	0.0004	9.89E-05	0.017	1	1	0.14	0.0043	0.86	0.0043
MR5766d	NNA 5766	0.011	0.0027	0.452	1	1	0.35	0.0226	0.65	0.0226
MR5713b	NNA 5613	0.008	0.0019	0.316	1	1	0.36	0.0188	0.64	0.0188
MR5713a	NNA 5613	0.0005	0.00013	0.022	1	1	0.12	0.0049	0.88	0.0049
MR5076a	NND 5076	0.006	0.0012	0.204	1	1	0.33	0.0151	0.67	0.0151
MR5077	NND 5077	0.007	0.0016	0.266	1	1	0.24	0.0173	0.76	0.0173
MR5076b	NND 5076	0.002	0.0004	0.072	1	1	0.19	0.0090	0.81	0.0090
MR5766b	NNA 5766	0.003	0.0008	0.129	1	1	0.11	0.0120	0.89	0.0120
reduced_CD1577	CD 1577	0.015	0.0025	0.419	1	1	0.65	0.0217	0.35	0.0217
oxidised_CD1577	CD 1577	0.003	0.0005	0.091	1	1	0.16	0.0101	0.84	0.0101
U(IV) Synthetic uraninite	(Tsarev et al., 2016)						1			
U(VI) Natural uranopilite	M 40774								1	

SI Table 9 Alternative EXAFS model using more MS paths

Sample	Ligand	N	R (Å)	ss (Å²)	ΔE_0	Red X²	r-factor	k-range (Å)	R-range (Å)	k-weighting	S0²
MR5766c	Oax2	1	1.75(4)	0.003 (fix)	7(1)	111	0.025	2 - 12	1.3 - 4	1,2,3	0.85
	Oax1	1	1.77(3)	0.003 (fix)							
	O15	2	2.20(1)	0.003 (fix)							
	O14	2	2.34(2)	0.003 (fix)							
	OH20	2	2.39(2)	0.003 (fix)							
	C	2	2.92(3)	0.003 (fix)							
	U-Oax2-U-Oax2 (MS)		3.51(6)	0.006 (fix)							
	U-Oax2-Oax1 (MS)		3.58(5)	0.006 (fix)							
	U-Oax2-U-Oax1 (MS)		3.58(5)	0.006 (fix)							
MR5713a	Oax2	1	1.77(10)	0.003 (fix)	9(3)	111	0.025	3 - 11.5	1.3 - 4	1,2,3	0.85
	Oax1	1	1.77(8)	0.003 (fix)							
	O15	2	2.23(5)	0.003 (fix)							
	O14	2	2.38(4)	0.003 (fix)							
	OH20	2	2.43(6)	0.003 (fix)							
	C	2	2.89(7)	0.003 (fix)							
	U-Oax2-U-Oax2 (MS)		3.54(11)	0.006 (fix)							
	U-Oax2-Oax1 (MS)		3.58(13)	0.006 (fix)							
	U-Oax2-U-Oax1 (MS)		3.58(13)	0.006 (fix)							
oxidised_CD1577*	Oax2	1	1.75(4)	0.003 (fix)	7(1)	111	0.025	2.5 - 12	1 - 4	1,2,3	0.85
	Oax1	1	1.77(3)	0.003 (fix)							
	O15	2.8(4)	2.20(1)	0.003 (fix)							
	O14	2	2.34(2)	0.003 (fix)							
	OH20	2	2.39(2)	0.003 (fix)							
	C	2	2.88(4)	0.003 (fix)							
	U-Oax2-U-Oax2 (MS)		3.50(6)	0.006 (fix)							
	U-Oax2-Oax1 (MS)		3.58(5)	0.006 (fix)							
	U-Oax2-U-Oax1 (MS)		3.58(5)	0.006 (fix)							

*these distances were constrained to be the same as those of MR5766c these 3 data sets were fitted together.

SI Figure 1 XRD spectra

A) Uranyl nitrate Patterns were collected with a Bruker D8 Advance Eco diffractometer equipped with a LYNXEYE XE linear position sensitive detector and using a Cu X-ray tube operated at 40 kV and 25 mA. Data were collected from 3–80° 2θ with a step size of 0.02°2θ and a counting rate of 1 s/step. Minerals were identified with reference to standard patterns from the ICDD Powder Diffraction File 2 (PDF-2) database using the DIFFRAC.EVA v.4 software package (available from Bruker AXS).

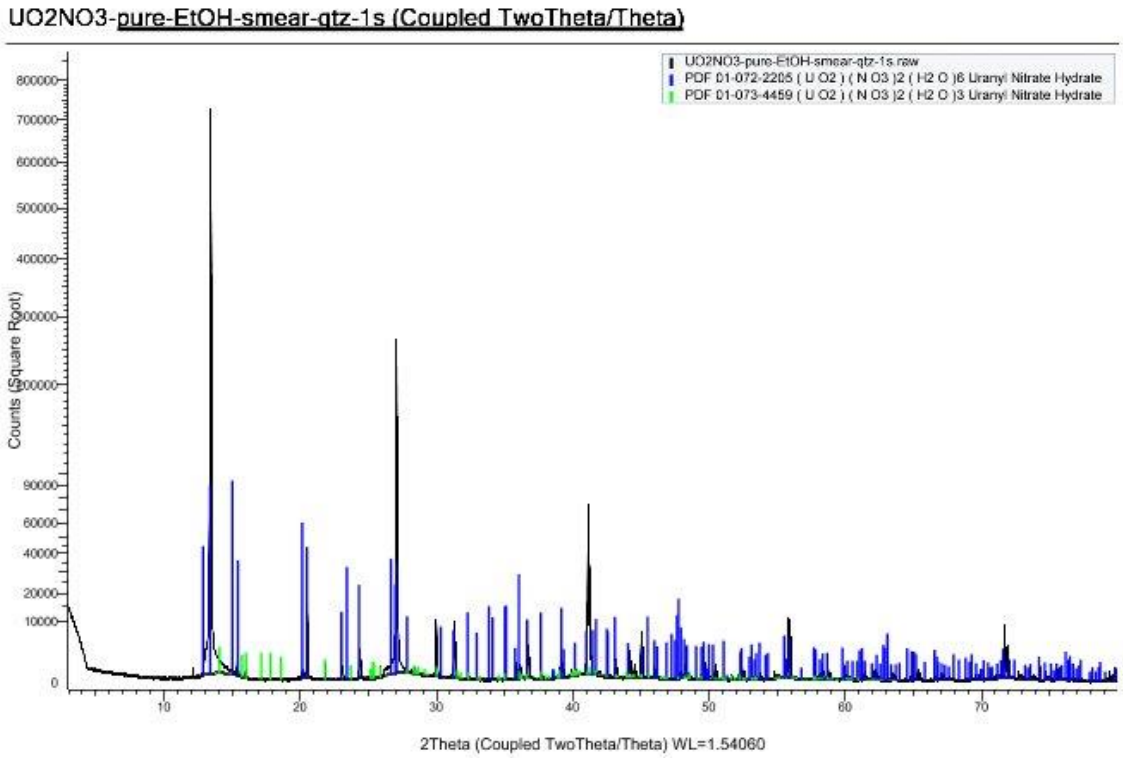

B) Background of CD1577. Data were measured using a Bruker GADDS microdiffractometer, using Cu Kα radiation from an X-ray tube operating at 40 mA, 40 kV. The incident beam was passed through crossed reflecting (Gobel) mirrors, resulting in a monochromatic, parallel, high-brilliance source which was then collimated through a 200 µm pinhole system. The spectrum was consistent with quartz alpha mixed with an unidentified minor phase.

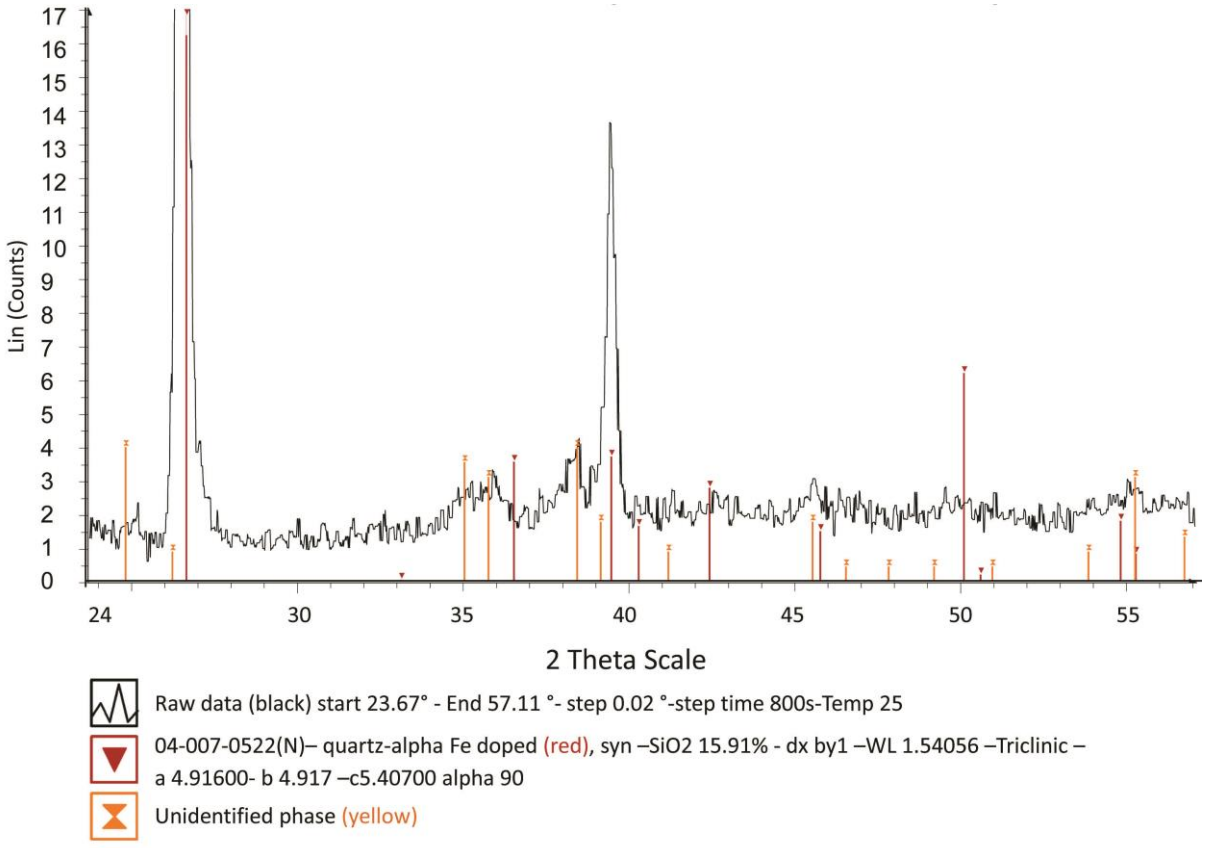

C) Coffinite- Micro-XRD pattern of mineralised area of uranium, spot analysis was taken at the edge of a pyrite grain. Red lines show markers corresponding to U(IV) coffinite pattern ($USiO_4$) (RRUFF). Beam = 300 µm Cu Kα collimator.

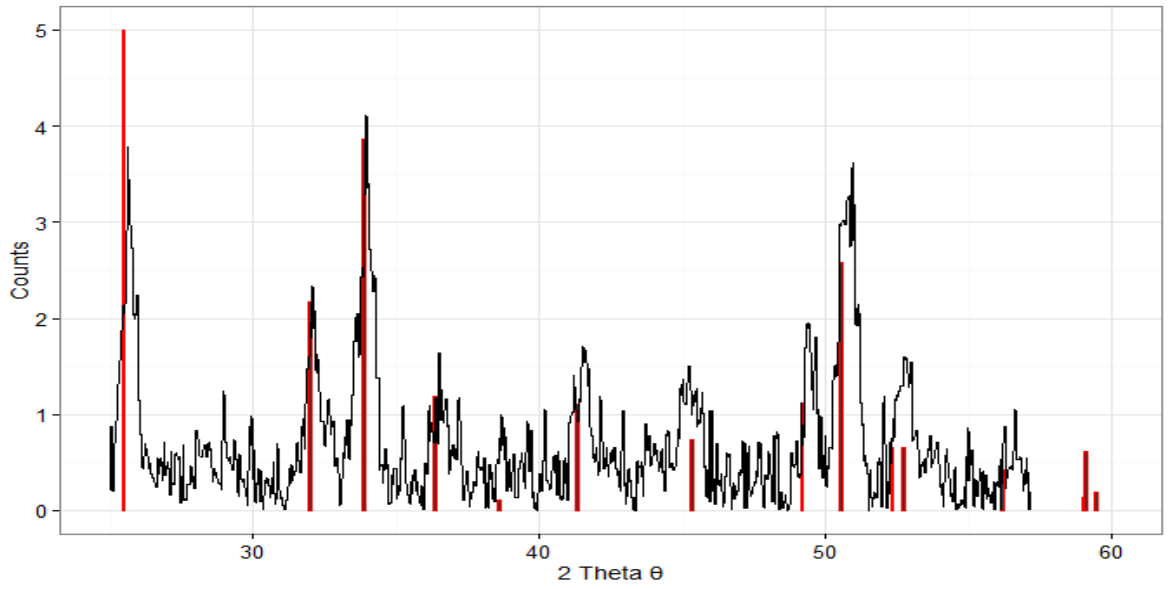

SI Figure 2 U L3 edge XAS x-ray absorption of the near edge structure for spectra of bulk cores and of some mineral standards

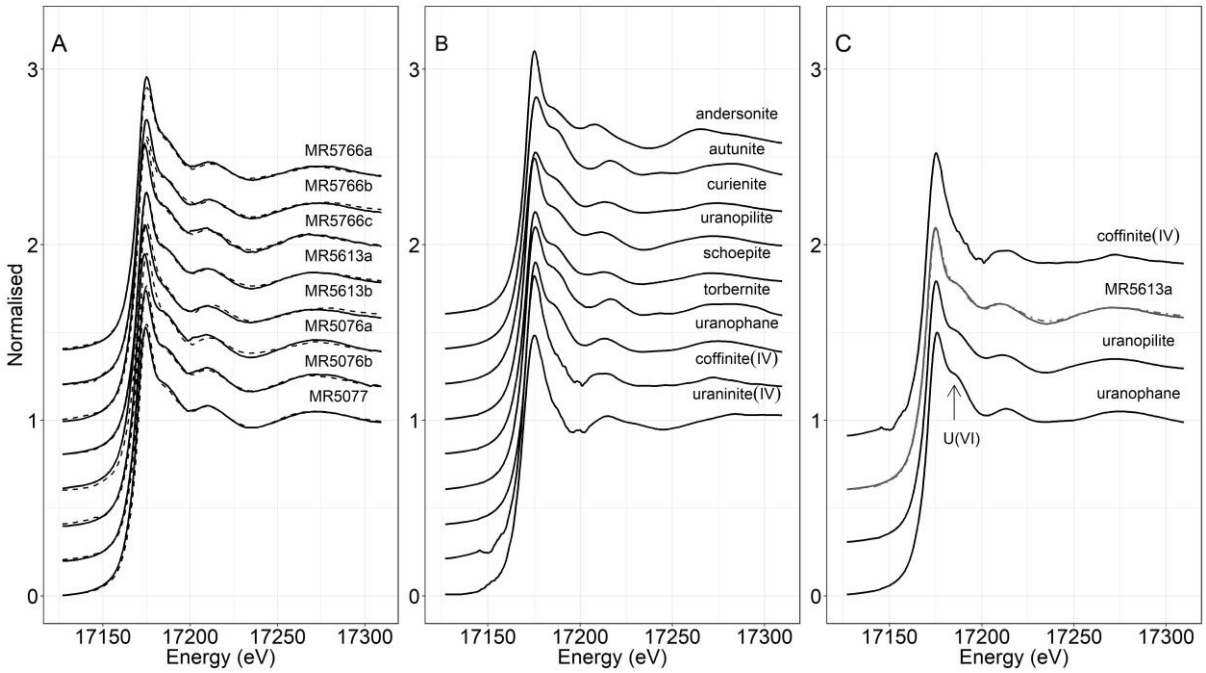

SI Figure 3 U L3 edge XAS - Extended x-ray absorbance of the fine structure shown in K^2 space. Top four spectra are fitted EXAFS of the bulk cores where solid line is the sample. The U(IV) and U(VI) lignite samples were from a thin section of MR lignite (CD 1577). The bottom seven spectra are mineral standards donated by Museum Victoria.

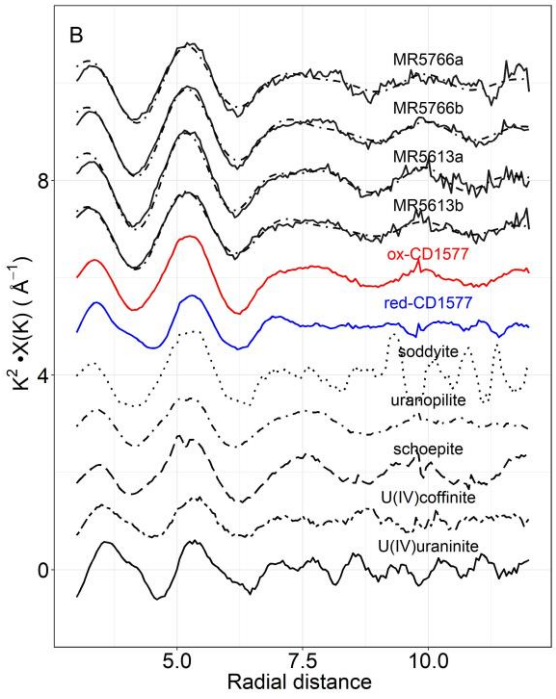

92 **SI Figure 4** EDS-SEM map and spectra from CD1577

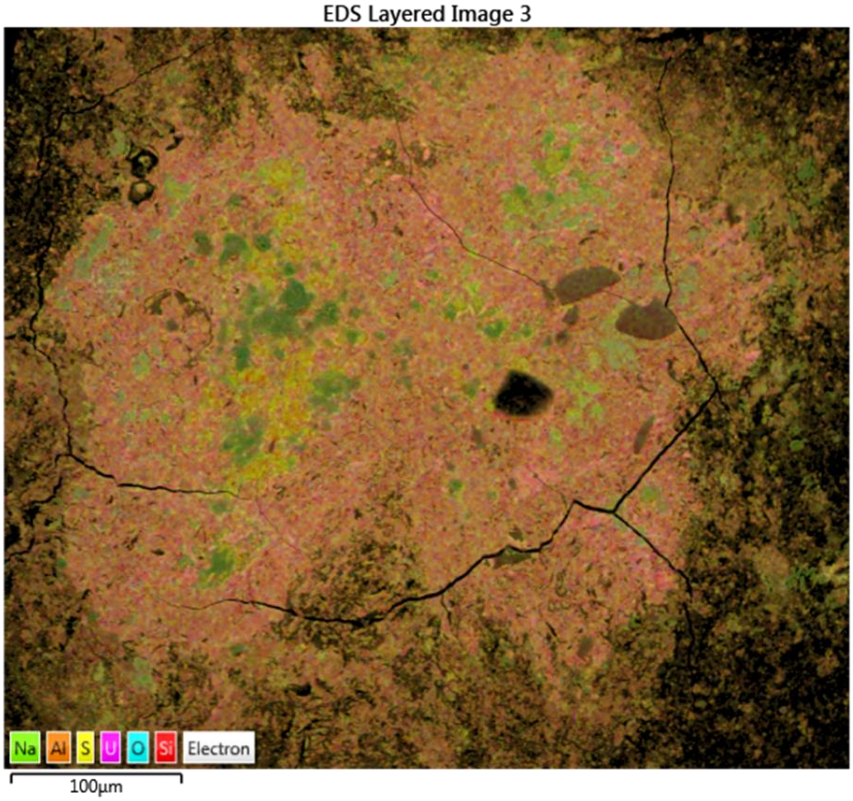

93

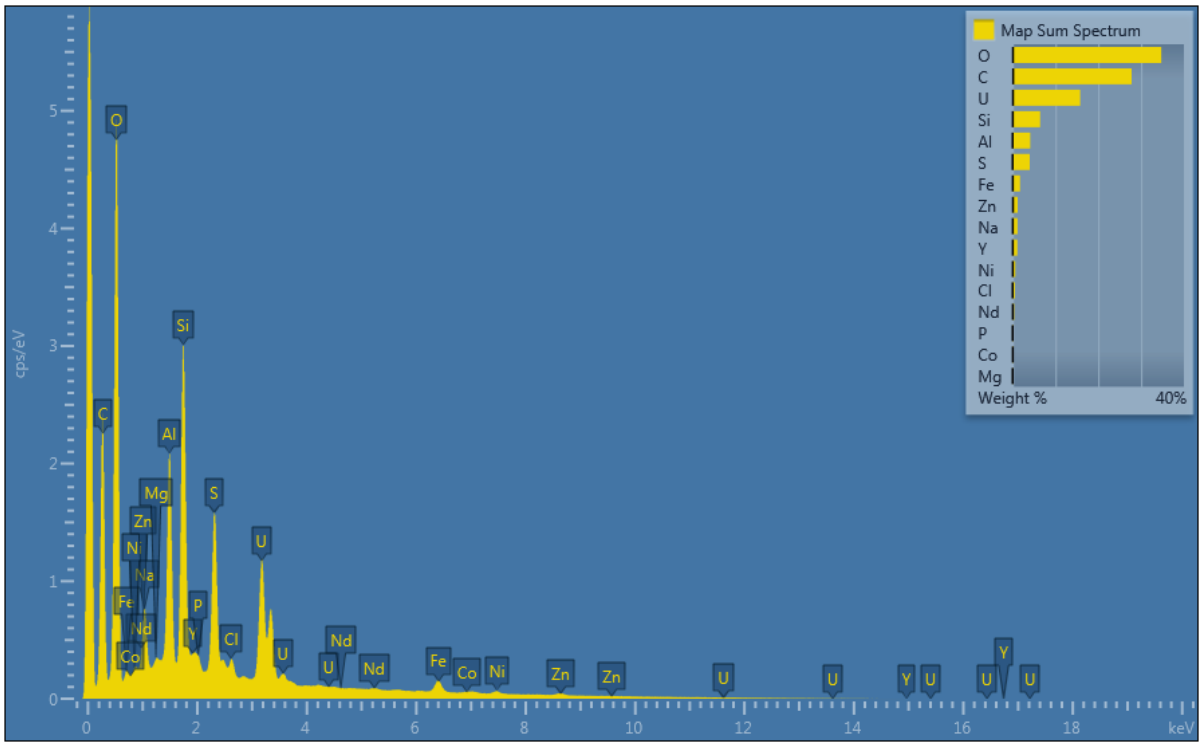

94

95